Hot electrons in nanoplasmonic devices

Submitted in partial fulfilment of the requirements for the degree of Doctor of Philosophy of Imperial College London and the Diploma of Imperial College London by

Hanwen Jin

Imperial College London

Department of Materials

May 2025

– Declaration of Originality –

Unless stated otherwise, this thesis is written by me under the supervision of Johannes Lischner. I wrote all the code that generated the data in the figures and drew all of the figures in this thesis.

– Copyright Statement –

– Abstract –

Localised surface plasmonic resonance is the oscillation of conduction electrons in metallic nanoparticles when it is illuminated with photons of a certain frequency. Nowadays, there is increasing effort to harness the energy or hot carriers from the metallic nanoparticles under plasmonic resonance. For example, researchers have used the plasmonic resonance effect to build photodetectors, photocatalysis, solar cells, etc. Despite the numerous experimental research, most theoretical studies are based on the classical approach such as solving Maxwell's equation. Little insights into the hot carriers are known as this is a quantum mechanical effect. To model the hot carriers, researchers have to solve Schrodinger's equation, which is computationally expensive. Researchers have attempted to model the hot-carrier processes using simplified wavefunctions such as the spherical-well approach, but this is less accurate and it is only limited to certain geometries of nanoparticles. Some other researchers uses ab-inito approaches to model these nanoparticles such as GW-perturbation method or time-dependent density functional theory calculations, but this can only be applied to very small ($\leqslant$2000 atoms) nanoparticles or bulk-like nanoparticles. In this research project, we used a semi-classical approach, we used the tight-binding method to compute the wavefunction of the nanoparticles and used the quasi-static method to compute the perturbation induced by the photon. We used an efficient kernel polynomial method that scales linearly with the number of atoms. We managed to simulate the hot carrier distribution of nanoparticles with from 249 atoms(~0.5 nm) up to 1,000,000 atoms(~30 nm). Based on the finite-element quasi-static method, we managed to calculate the classical potential for arbitrary geometry. This allows us to calculate the hot-carrier generation rate of more complicated structures, such as Au@Pd core-shell nanoparticle surrounding a big Au nanoparticle and metallic Janus nanoparticles with a neck.

– Acknowledgements –

I would like to express appreciation to:

- My supervisor **Johannes Lischner**, who gave me the initial direction of PhD research. Without choosing the correct direction, I cannot publish my work in these prestigious journals. He has also contributed significantly to analysing the data I have generated, correcting the grammatical errors I have made and helping me draft this thesis's structure.

- My second supervisor **Arash Mostofi** and his student **Chengcheng Xiao**, I have had a lot of discussions with them in terms of technical questions; they have also contributed significantly towards the density functional fitting algorithm that was used in section 5.

- **Simao Joao**, who joined the discussion with me in the group meeting of plasmonic hot-carrier generations. These discussions provided a lot of inspiration that positively impacted this thesis.

- **Valerio Vitale**, who provided me with the LaTeXcode for generating all the reference sections, without this code, all the research cannot get published in Arxiv.

- All other collaborators I collaborated with during my PhD.

- **My family** who have supported my financially and spiritually.

- **Department of Materials**, Imperial College London, I have completed my undergraduate and doing Postdoctoral studies here; the undergraduate program provides me with a solid basis for solid-state physics and materials modelling. My thesis writing skill was also enhanced during my undergraduate study at the Department of Materials.

- **Department of Mathematics**, Imperial College London, I have computed my master of science (MSc) programme here, the course I learned from here provides me with a solid basis for physics, numerical methods and computational programming. In particular, half of the section 2 is directly or indirectly related to the content I studied at the Department of Mathematics.

– Contents –

– List of Figures –

– List of Tables –

– List of Acronyms –

LSP	Localised Surface Plasmon
DFT	Density Functional Theory
TDDFT	Time-dependent Density Functional Theory
GW	One Particle Green's Function And Screened Columb Interaction
TB	Tight Binding
QS	Quasi Static

Chapter 1

Introduction and Background

1.1 Fundamental Hot Carrier Processes

Nowadays, with the advances of nanotechnology, a wide range of nanoparticles, which have a typical length scale of less than 100 nm, can be synthesisedd. These nanoparticles have a wide range of sizes, shapes and compositions.[1] It is well known that nanoparticles have significantly different optical properties from their bulk materials. For example, depending on the shape and size of gold nanoparticles, they show significantly different colours. [2] This is attributed to the localised surface plasmon resonance effect. When a metallic nanoparticle is illuminated with light, the collective oscillation of the electric field creates a plasmon, which is confined in a sub-wavelength region by the nanoparticle. It is called localised surface plasmon (LSP)[3, 4, 5, 6, 7]. The LSP is illustrated in Figure 1.1. Due to the many-body nature of these LSPs, they possess a finite lifetime. The LSP has two main decay mechanisms: one is by emission of light, and the other is by decaying into energetic hot carriers via Landau damping[8].

1.2 Experimental Study of Localised Surface Plasmon

Over the past few decades, researchers have developed a wide range of experimental techniques to synthesise and characterise plasmonic nanoparticles, as well as use them to make new optoelectronic devices. The fabrication technique includes milling[9], lithography[10], Turkevich method(reduction of $HAuCl_4$)[11], vapour-liquid-solid method[12] and scanning probe methods. [13] These methods allow researchers to synthesise nanoparticles with sizes ranging from a few nanometers to a few micrometres. Researchers also have a lot of techniques to

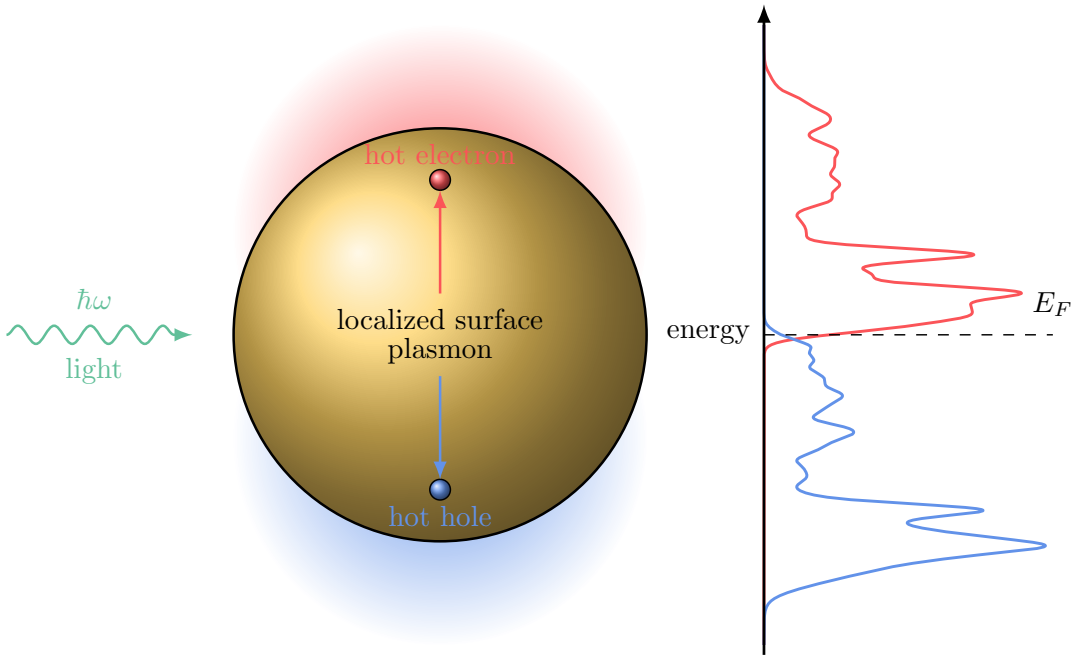

Figure 1.1: Schematic illustration of the hot carrier generation process

characterise the nanoparticle they synthesised. The characterisation methods for nanoparticle shape, composition and crystallography include scanning electron microscopy(SEM)[14], transmission electron microscopy (TEM)[15] and X-ray diffraction (XRD).[16] The methods to characterise the plasmonic properties include UV-visible spectroscopy[17], pump-probe spectroscopy[18], as well as measuring the performance of plasmonic materials in the optoelectronic devices. Based on these characterisation techniques, researchers found that gold, silver and copper are the most important plasmonic materials, as these materials have a completely filled d-band, and they are less likely to undergo s-d interband transition (which leads to Ohmic losses). In general, gold and silver have a better plasmonic performance, but copper has a cheaper cost and is easier for industrial-scale fabrication. [4] In this research, we will thus focus on these materials, but the method developed can be generalised to any other materials.

In terms of applications of LSP, in the early stages, researchers were interested in using the scattering mechanism to harness the energy from the LSP. They built a layer of nanoparticles, which scatters the light into the active layer of the solar cells[3, 19]. In recent years, the idea of harnessing the energy from the energetic 'hot' carrier from the decay of localisedd surface plasmon is becoming more popular[20, 21]. For example, a gold nanoparticle can help split water into hydrogen and oxygen under the illumination of solar radiation. (they are called hydrogen evolution reaction and oxygen evolution reaction, respectively) Without these photonic catalysts, these reactions require high temperature or pressure[22], and the

hydrogen created can be used as a clean fuel. Similarly, these energetic hot carriers have been used to catalysee carbon dioxide reduction reactions.[23, 24, 25, 26]. In addition, based on the optical properties of plasmonic materials, researchers have developed some photodetection devices. [27, 28, 29, 30, 31, 32, 33]

1.3 Previous Approaches for Modelling Hot Carriers

Despite the numerous successes in harnessing the energy from localised surface plasmons, the efficiency of nanoplasmonic devices remains much lower than the theoretical value. [34, 35] This is because researchers do not have a thorough understanding of the process behind the hot-carrier generation. In particular, the relationship between the shape, composition and performance of these plasmonic nanomaterials remains unclear. Apart from that, researchers are unclear whether the catalytic effect observed is attributed to the local heating from the hot carrier or the charge transfer. [36, 37, 38, 39, 40]. In addition, there is no theoretical model that describes the relationship between sharp features and the performance of plasmonic devices. Thus, developing a theoretical formalism to model these hot carrier generation processes becomes increasingly important.

The plasmonic properties of the materials are governed by the many-body Schrödinger's equation[41]:

$$\hat{H}\psi = E\psi, \tag{1.1}$$

where the Hamiltonian operator $\hat{H}$ can be expressed as[1]

$$\hat{H} = \sum_i \nabla^2_{\mathbf{r}_i} + \sum_{i \neq j} \frac{1}{|\mathbf{r}_i - \mathbf{r}_j|} + \hat{V}_{\text{nuclei}} \tag{1.2}$$

Schrödinger's equation contains a Coulomb repulsion term $\frac{1}{|\mathbf{r}_i - \mathbf{r}_j|}$, which makes solving Schrödinger's equation numerically very challenging. [42] The computation cost grows exponentially with the system's size. Because of this, researchers have not solved the complete Schrödinger equation numerically beyond 10 electrons. A widely used material modelling method is based on density functional theory (DFT). Instead of solving the many-electron Schrödinger equation directly, DFT reformulates the problem in terms of electron density. (Which makes the calculation scale cubically or less [43]) This is achieved through the Kohn-Sham equations, which describe a system of non-interacting electrons that reproduce the same electron density as the real system. The exchange-correlation energy, which accounts for quantum mechanical effects, is approximated using exchange-

[1] Written in atomic unit

correlation functionals. This makes DFT computationally efficient and often in good agreement with experimental results. However, density functional theory can only model the ground state of materials, and modelling localised surface plasmon involves excited state calculations.[41] In this section, we will go through the computational method, starting from the most computationally demanding one (the GW method) to the least computationally demanding one (the spherical well method).

The most accurate way of modelling the hot-carrier process is to use GW methods. This method starts with a density functional theory calculation and then approximates the self-energy Σ of the system in terms of the product of one-body Green's function G and screened Coulomb interaction W (i.e. $\Sigma = iGW$). [44] This method is also capable of calculating the lifetime of charge carriers as the self-energy term is a non-Hermitian, and the imaginary part of the self-energy is the lifetime. This method is so computationally demanding that it has been rarely applied to nanoparticles. [45] The GW method can also be used for calculating the electron-plasmon coupling constant that has been used to parameterise an effective Hamiltonian that is much easier to solve. [46]

A less computationally demanding method is time-dependent density functional theory (TDDFT). This method uses the ground state wavefunction from a standard DFT calculation and then computes the time evolution of the electron density under the influence of the external electric field. This method is more scalable (it has been applied to a silver nanoparticle containing 561 atoms) and more flexible (it can be used to model a wider range of geometries). [47, 48, 49, 50, 51] However, the hot-carrier distribution depends sensitively on the size of systems. A typical nanoparticle used in optoelectronic devices is larger than 10 nm in size, and it cannot be modelled using the TDDFT approach. Moving on to more simplified methods, researchers use the jellium model (uniform electron gas model) [46, 52] or spherical well model[53] to describe the wavefunction of electrons. The electric field was treated using Fermi's golden rule. For systems with spherical symmetry, these methods show great scalability. Taking the spherical well model as an example, the wavefunction can be written in terms of the products of the spherical Bessel functions and spherical harmonics. [54] The overlap integral of different eigenstates of the Hamiltonian with the perturbation potential can be computed easily. As a result, these methods have been used to model nanoparticles with diameters up to 30 nm. Note that core-shell nanoparticles also have spherical symmetry. The core-shell nanoparticle has also been studied by this method in 2018[55]. In addition to the fact that these methods have certain restrictions on the symmetry of the system that can be studied, they are also only capable of

modelling s-p bands. In 2020, researchers combined the spherical well model with the envelope function method to model a *flat* d-band[56], but in reality, these transition metals do not have flat d-bands(see figure 3.2 in section 3) and hence using this assumption to model hot-carrier process is not very accurate.

Table 1.1: Comparison of the theoretical approaches to model hot-carrier processes.

	speed	flexibility	accuracy
GW method	low	low	high
TDDFT	medium	high	medium
Spherical well model	high	medium	low

The goal of this project is to develop a computational method that is capable of having ab-initial accuracy(similar to the TDDFT and GW methods), having the scalability of the spherical well model and the flexibility of the TDDFT method.

1.4 Approaches for Modelling Large Systems

The tight-binding method is a way of writing Schrödinger's equation in the basis of localised atomic orbitals. [57] It treats the interaction of different atomic orbitals as a perturbation. The tight-binding parameters are fitted from more advanced calculation methods such as density functional theory, GW theory or experimental results. [58, 59] This method is much more robust compared to the more advanced methods, but it gives numerically correct results in many scenarios. Using this technique, the dimension of the Hilbert space is reduced significantly, and one can solve Schrödinger's equation for a 3,000-atom nanoparticle on a laptop. However, the cubic scaling nature of diagonalisation makes it difficult to scale the problem further. A nanoparticle with a diameter of 10 nm contains 30,000 atoms. This is impossible to handle with a standard laptop. Fortunately, in the tight-binding picture, the interaction between neighbouring atoms decays rapidly with distance, [60]. In many tight-binding models that can be found in the literature, the interaction terms were set to zero after the second nearest neighbour. [61] This makes the tight-binding Hamiltonian sparse. There are many nice properties of a sparse matrix. For example, the matrix-vector product of a sparse matrix scales linearly with the Hilbert space dimension. With this in mind, researchers have written the density of states. This typical spectral quantity can be measured experimentally or calculated from a more advanced method, in terms of the trace of Chebyshev polynomial expansion of the spectral operator $\delta(E - \hat{H})$. Expanding a highly discontinuous function like the Dirac-delta function will introduce unphysical Gibbs oscillation, which is damped by convoluting it

with a kernel. [62, 63, 64, 65, 66]. This technique of writing spectral quantities in terms of the spectral operator and evaluating them using a linear scaling algorithm was termed the Kernel Polynomial method. [67] Using this method, researchers have successfully evaluated the electrical conductivity, projected density of states, phonon lifetime and many other quantities for systems containing up to 10 billion (10^{10}) atoms. However, this method has not yet been applied to the plasmonic system. The goal of this project is to generalise the formalism of the kernel Polynomial method to calculate the hot-carrier generation rate and use this method to model the hot-carrier generation in a wide variety of nanoparticles.

1.5 A Brief Overview of the Thesis

In chapter 2, we will develop a theoretical framework of the mathematical theory behind the linear scaling algorithm used in this project, and we will discuss how different convergence parameters impact the accuracy and resolution of our model. In chapter 3, we used the method to model spherical nanoparticles with up to 1 million atoms and discuss the contribution of interband and intraband transitions to the hot-carrier generation rate. In chapter 4, we used the method to model the hot-carrier generation rate of an antenna and satellite system. In chapter 5, we used the algorithm to model spherical and dumbell-shaped Janus nanoparticles.

1.6 Publications

Most of the content in this thesis has been submitted for publication. In particular:

1. The materials presented in chapter 3 has been published in PRX Energy, entitled: 'Plasmon-Induced Hot Carriers from Interband and Intraband Transitions in Large Noble Metal Nanoparticles'. [68]
2. The materials presented in chapter 4 has been published in ACS Photonics, entitled: 'Theory of Hot-Carrier Generation in Bimetallic Plasmonic Catalysts'.[69]
3. The materials presented in chapter 5 has *not* been published, as I decided to run additional calculations.

In addition, I have contributed to the following thesis.

1. The linear-scaling algorithm used in this thesis has been modified and used to calculate the steady-state hot-carrier distribution. This work was published in The Journal of Physical Chemistry C, entitled 'Atomistic Theory of Hot-Carrier Relaxation in Large Plasmonic Nanoparticles'.[70]
2. The distance-dependent tight-binding code I have written based on reference [146] was used to calculate the hot-carrier distribution of Au-Ag alloy nanoparticle. This work was published in Communication Chemistry, entitled 'Hot carriers from intra- and interband transitions in gold-silver alloy nanoparticles'. [71]

Chapter 2

Methods

In this chapter, we introduce our approach for modelling plasmonic nanoparticles, which is based on the tight-binding method and the kernel polynomial method (KPM). Combining these two methods allows one to model experimentally relevant plasmonic nanoparticles on a laptop. In this section, we will first introduce how to represent the wavefunction of the plasmonic materials in the tight-binding picture; next, we will derive the equation for the hot-carrier distribution in the tight-binding form, which contains a Hamiltonian term and a perturbation term. After that, we will look at how to obtain the tight-binding Hamiltonian and the perturbation term. And finally, we will use KPM to simplify the calculation.

2.1 Tight-binding Method

2.1.1 Second Quantisation

To describe the wavefunction, we assume that the electrons are strongly localised in their atomic orbital. So we write the wavefunction in the basis of atomic orbitals. We write the equation in terms of second quantisation, e.g. for a system with an s-orbital and a p-orbital

$$|\psi\rangle = (\psi_s \hat{c}_s^\dagger + \psi_p \hat{c}_p^\dagger)\,|0\rangle \mapsto \begin{pmatrix} \psi_s \\ \psi_p \end{pmatrix}, \tag{2.1}$$

where $\hat{c}_\alpha^\dagger$ is the creation operator, which creates an electron at orbital $\mathfrak{i}$ in the vacuum state $|0\rangle$. Its adjoint operator $\hat{c}_\alpha$ is the annihilation operator.[72, 73, 74, 75]

The creation and annihilation operators satisfy

$$\{\hat{c}_\alpha, \hat{c}_\alpha^\dagger\} = \hat{c}_\alpha \hat{c}_\alpha^\dagger + \hat{c}_\alpha^\dagger \hat{c}_\alpha = 1, \tag{2.2}$$

$$\hat{c}_\alpha |0\rangle = 0. \tag{2.3}$$

Hence,

$$\hat{c}_\alpha \hat{c}_\alpha^\dagger |0\rangle = 1 |0\rangle . \tag{2.4}$$

Using the second quantisation notation, we can write the wavefunction as

$$|\psi\rangle = \sum_\alpha \psi_\alpha \hat{c}_\alpha^\dagger |0\rangle . \tag{2.5}$$

2.1.2 Tight-binding Hamiltonian in Second Quantisation

The Schrödinger equation in the tight-binding formalism can be written as [57]

$$\hat{H} |\psi\rangle = \left(\sum_{\alpha\mathbf{R}} \varepsilon_\alpha \hat{c}_{\alpha\mathbf{R}}^\dagger \hat{c}_{\alpha\mathbf{R}} + \sum_{\alpha\mathbf{R},\ \beta\mathbf{R}'} t_{\alpha\mathbf{R},\beta\mathbf{R}'} \hat{c}_{\alpha\mathbf{R}}^\dagger \hat{c}_{\beta\mathbf{R}'} \right) |\psi\rangle = E |\psi\rangle , \tag{2.6}$$

where $\mathbf{R}$ and $\mathbf{R}'$ label the atoms, α and β label the orbitals, the diagonal term in the matrix $\sum_\alpha \varepsilon_\alpha \hat{c}_\alpha^\dagger \hat{c}_\alpha$ accounts for the onsite energy of the atomic orbitals and the off-diagonal term $\sum_{\alpha,\beta} t_{\alpha\beta} \hat{c}_\alpha^\dagger \hat{c}_\beta$ accounts for the hopping energy of the system.

There are two approaches to finding the onsite energy ε and hopping energy t. One approach is to construct maximally localised Wannier functions from a density functional theory calculation. However, the tight binding parameters produced by this method decay very slowly with distance. As we will show later, the Hamiltonian must be sparse to make our algorithm linearly scaling. The other set of methods introduced by Slater and Koster[58] is based on fitting the so-called "Slater-Koster parameters" based on the band structure of the bulk material. The hopping parameters calculated with this method decay quickly with distance. As an example, the s-p hopping between two atoms is given by

$$t_{s,p_x} = l V_{sp\sigma}, \tag{2.7}$$

the hopping between s and d_{z^2} is given by

$$t_{s,3z^2-r^2} = [n^2 - (l^2 + m^2)/2] V_{sd\sigma}, \tag{2.8}$$

where $V_{sp\sigma}$ and $V_{sd\sigma}$ are the Slater-Koster parameters and l, m and n are the direction cosine(in the x, y and z-direction respectively). One can find the full Slater-Koster table in the following reference[58, 59].

2.1.3 Fitting the Tight-binding Parameters

In this section, we will introduce how Slater-Koster parameters are fitted. We first need to introduce Bloch's theorem, which says that if the Hamiltonian is invariant under a translation,

$$\hat{T_{\mathbf{A}}}^{-1}\hat{H}\hat{T_{\mathbf{A}}} = \hat{H} \tag{2.9}$$

where $\mathbf{A} = n_0\mathbf{a}_0 + n_1\mathbf{a}_1 + n_2\mathbf{a}_2$ is the lattice vector ($n_0, n_1, n_2 \in \mathbb{Z}$), then the Hamiltonian can be transformed into a block diagonal form

$$\hat{H} \sim \begin{bmatrix} \hat{H}(\mathbf{k}_0) & \hat{0} & \cdots & \hat{0} & \hat{0} \\ \hat{0} & \hat{H}(\mathbf{k}_1) & \cdots & \hat{0} & \hat{0} \\ \vdots & \ddots & \ddots & \ddots & \vdots \\ \hat{0} & \hat{0} & \cdots & \hat{H}(\mathbf{k}_{N-2}) & \hat{0} \\ \hat{0} & \hat{0} & \cdots & \hat{0} & \hat{H}(\mathbf{k}_{N-1}) \end{bmatrix}, \tag{2.10}$$

where

$$\hat{H}(\mathbf{k}_n) = \sum_{\alpha\mathbf{0}} \varepsilon_\alpha \hat{c}^\dagger_{\alpha\mathbf{0}}\hat{c}_{\alpha\mathbf{0}} + \sum_{\alpha\mathbf{0},\ \beta\mathbf{R}'} t_{\alpha\mathbf{0},\beta\mathbf{R}'}\hat{c}^\dagger_{\alpha\mathbf{0}}\hat{c}_{\beta\mathbf{R}'}e^{2\pi i\mathbf{k}_n\cdot\mathbf{R}'}. \tag{2.11}$$

In this equation, $i = \sqrt{-1}$ is the complex unity, and the number of $\mathbf{k}$-points depends on the size of the supercell we choose. If we make a super-cell with periodic boundary conditions containing $N = N_{\mathbf{a}_0} \times N_{\mathbf{a}_1} \times N_{\mathbf{a}_2}$ unit cells, then there are $N = N_{\mathbf{a}_0} \times N_{\mathbf{a}_1} \times N_{\mathbf{a}_2}$ $\mathbf{k}$-points in the reciprocal space. They are

$$\mathbf{k}_n = \sum_{i=0}^{2} \left(\frac{n_i}{N_{\mathbf{a}_i}} - \frac{1}{2}\right)\mathbf{b}_i, \quad \forall n_i \in [0, N_{\mathbf{a}_i}), \tag{2.12}$$

where $\mathbf{b}_i = \frac{\mathbf{a}_j \times \mathbf{a}_k}{|\mathbf{a}_i \cdot (\mathbf{a}_j \times \mathbf{a}_k)|}$ is the reciprocal lattice vector. This is the Monkhorst-Pack k-point mesh. [76]

Now, $H(\mathbf{k})$ has the same Hilbert space dimension as the atom at the origin. For the plasmonic materials, like gold, silver, and copper, we chose the spd orbital set with nine orbitals. $\hat{H}(\mathbf{k})$ can be solved by

$$\hat{H}(\mathbf{k})\,|n\mathbf{k}\rangle = E_{n\mathbf{k}}\,|n\mathbf{k}\rangle\,. \tag{2.13}$$

To solve equation 2.13 in the DFT picture and find $E_n^{DFT}(\mathbf{k})$, we used Vienna Ab initio Simulation Package(VASP)[77, 78], a popular plane-wave DFT package

with Perdew-Burke-Ernzerhof (PBE) exchange-correlation potential [79] with a wavefunction cutoff of 500 eV. To find the equilibrium lattice constant of each material, we use the conjugate-gradient algorithm with an $8\times8\times8$ Monkhorst-Pack k-points mesh to relax the structure until the force between atoms is less than 0.001 eV/ Å. We strain the lattice using the algorithm discussed in the previous section. To find $E_n^{DFT}(\mathbf{k})$ for each strained structure, we run an initial DFT calculation with a $8 \times 8 \times 8$ Monkhorst-Pack k-points mesh followed by a non-self-consistent calculation with $10 \times 10 \times 10$ Monkhorst-Pack k-points mesh.

To fit the tight-binding parameters, we calculate $E_{n\mathbf{k}}^{DFT}$ as discussed above. We want to find the best tight-binding parameters $\left(\mathbf{V}^*_{\alpha\beta\eta}; \mathbf{E}_{s/p/d}\right)$, where $\mathbf{V}^*_{\alpha\beta\eta}$ represent the vector of Slater-Koster hopping parameters and $\mathbf{E}^*_{s/p/d}$ represents the onsite energy and the superscript * means the optimal parameters. We define the fitting error for a given set of parameters $\mathbf{V}_{\alpha\beta\eta}$ and $\mathbf{E}_{s/p/d}$ to be

$$\text{error}\left(\mathbf{V}_{\alpha\beta\eta}; \mathbf{E}_{s/p/d}\right) = \sum_{n\mathbf{k}} \left(E_{n\mathbf{k}}^{DFT} - E_{n\mathbf{k}}^{TB}\left(\mathbf{V}_{\alpha\beta\eta}; \mathbf{E}_{s/p/d}\right)\right)^2, \tag{2.14}$$

and $\mathbf{V}^*_{\alpha\beta\eta}$ and $\mathbf{E}^*_{s/p/d}$ are given by

$$\mathbf{V}^*_{\alpha\beta\eta}, \mathbf{E}^*_{s/p/d} = \underset{\mathbf{V}_{\alpha\beta\eta}, \mathbf{E}_{s/p/d}}{\text{argmin}} \left(\text{error}\left(\mathbf{V}_{\alpha\beta\eta}; \mathbf{E}_{s/p/d}\right)\right) \tag{2.15}$$

We start with the Slater-Koster parameters from the literature [59] and use them as an initial guess, and we use the Levenberg-Marquardt least-square minimisation technique [80] to minimise the error. To visualise the goodness of fitting, we computed the band structure of gold using VASP. We conducted a self-consistent field calculation using the method discussed above for visualisation purposes; we then computed the eigenvalue along a high-symmetry path using the non-self-consistent field calculation. We compared the tight-binding energy with that calculated from VASP. We plotted them in figure 2.1, and it can be seen that the results from density functional theory and tight-binding are in good agreement.

2.2 Constructing the Nanoparticle.

In this project, we work with nanoparticles that do not have periodic structures or unit cells like the other tight-binding code[62, 81]. To automate the construction process, we must develop a method to carve the nanoparticle from the bulk material. However, a bulk material has infinite atoms, while a computer can handle only a finite number of atoms(deciding if an atom lies inside a shape needs

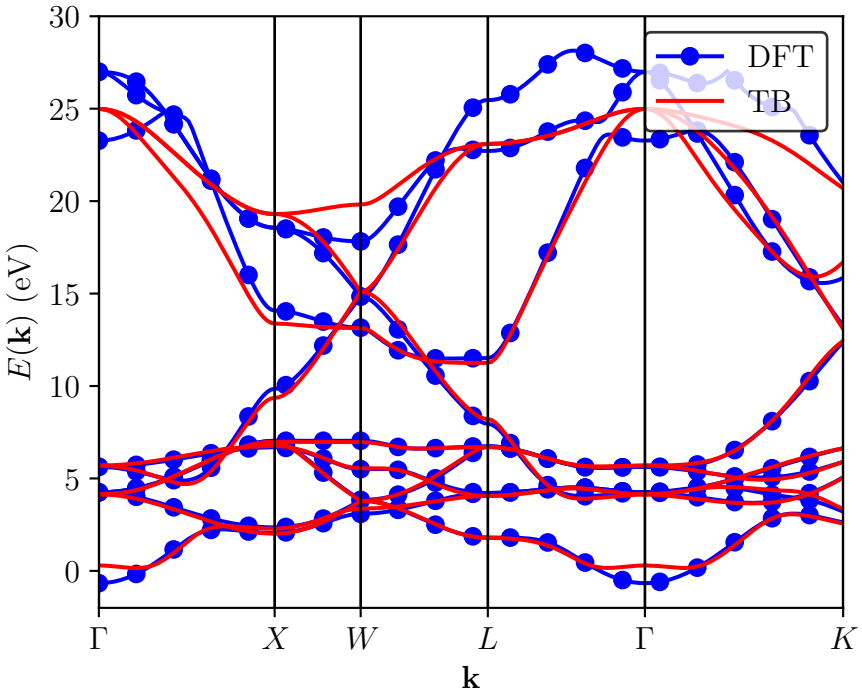

Figure 2.1: Schematic illustration of the Band structure of bulk gold atom computed using Density functional theory and the band structure fitted with Levenberg-Marquardt least-square minimisation methods.

some computation power). Some researchers pre-define a very large supercell to ensure all the atoms inside the nanoparticle are included in the large supercell, but this requires a huge amount of computational power, or some atoms inside the nanoparticle will not get carved. To resolve this problem, we developed an algorithm that can efficiently achieve the cutting process for an arbitrary shape. For each shape, we define a function `inShape` that returns a `list` of `True` or `False` based on the input positions. We start with a small supercell (a $\times$ a $\times$ a, centred in origin) based on the initial unit cell. We compute the number of in-shape atoms from `inShape` function; we then compare the number of in-shape atoms from a slightly bigger supercell and check if the in-shape atoms converge. If not, we double the number of atoms in the x, y and z directions and repeat the process (a $= 2 \times$ a $+ 1$). We repeat the process until the process converges. The flow chart of the building algorithm is shown in Figure 2.2

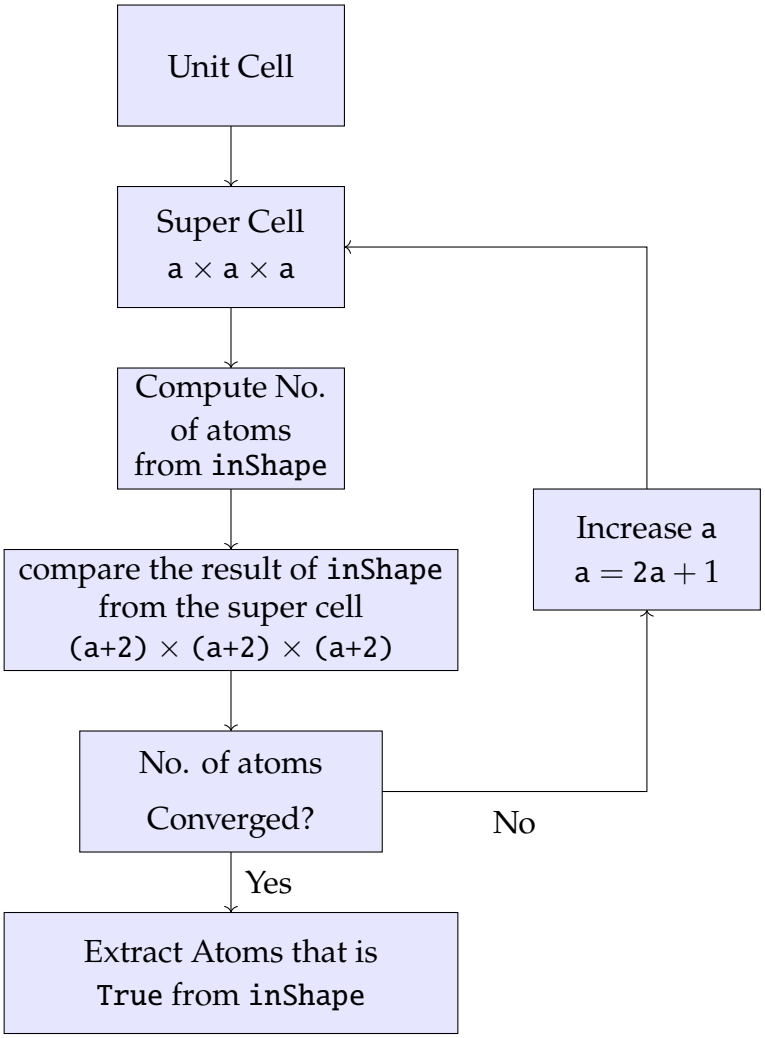

Figure 2.2: Schematic illustration of the algorithm used to carve the nanoparticle from bulk metal.

2.3 Fermi's Golden Rule

2.3.1 Hot Carrier Generation Rate

Suppose the nanoparticle is in its ground state and at $t = 0$, a perturbation $\hat{\Phi}(\omega, r, t) = e^{i\omega t}\hat{\Phi}(\omega, r)$ interacts with the system. In the steady state ($t \to \infty$), the probability for an electron to start in state $|E_i\rangle$ and end up in state $|E_f\rangle$ is given by

$$N_e(E, \omega) = \sum_{i,f} \left|\langle E_i| \hat{\Phi}(\omega, r) |E_f\rangle\right|^2 \delta(E_i - E_f - \hbar\omega; \gamma)\delta(E - E_f; \sigma)F(E_f)(1 - F(E_i)). \tag{2.16}$$

Here, $\delta(x; \sigma)$ is a Gaussian broadened Dirac-delta function, σ is the electron lifetime, γ is the transition broadening parameter which reflects the linewidth of an electron-hole pair excitation[1] and $F(E) = \frac{1}{1+exp\left(\frac{E-E_F}{kT}\right)}$ is the Fermi-Dirac distribution. [82, 83] [2] Unless stated otherwise, we choose $\sigma = 0.06$ eV, $\gamma = 0.05$ eV and $T = 300$ K in this thesis.

A similar expression exists for the holes, and it is given by

$$\begin{aligned} N_h(E, \omega) = &\sum_{i,f} \left|\langle E_i| \hat{\Phi}(\omega, r) |E_f\rangle\right|^2 \delta(E_i - E_f + \hbar\omega; \gamma) \\ &\delta(E - E_i; \sigma)F(E_i)(1 - F(E_f)). \end{aligned} \tag{2.17}$$

[1] Here we have used typical values for the broadening parameters σ and γ based on our previous work which in detail studied the effect of electron-electron and electron-phonon interactions [53]. We have verified that the calculated hot-carrier generation rates are not sensitive to the precise values of the broadening parameters.

[2] For a continuous wave photocatalysis experiment, the electron occupation will not necessarily follow a Fermi-Dirac distribution. However, calculating the full non-equilibrium distribution function would require a detailed theory of relaxation effects, which goes beyond the scope of this PhD project. These non-equilibrium distribution was discussed in reference [70] after the content of chapter 4 gets published. Fermi's Golden Rule was evaluated using other distributions than Fermi-Dirac in Refs. [92, 93].

2.3.2 Quasi-static Potential

We calculate the potential $\hat{\Phi}(\omega, r)$ in the quasi-static approximation[84, 85, 86, 87, 88, 89]. The potential Φ is governed by the Maxwell's equation[90, 91],

$$\nabla \cdot \mathbf{E} = \frac{\rho}{\epsilon} \tag{2.18}$$

$$\nabla \cdot \mathbf{B} = 0 \tag{2.19}$$

$$\nabla \times \mathbf{E} = -\frac{\partial \mathbf{B}}{\partial t} \tag{2.20}$$

$$\nabla \times \mathbf{B} = \mu(\mathbf{J} + \epsilon \frac{\partial \mathbf{E}}{\partial t}) \tag{2.21}$$

We assume that the nanoparticle is much smaller than the wavelength of the light($\lambda \gg a$, where a is the characteristic size of the system). With this approximation, we can assume that the light phase is constant in the whole nanoparticle volume. We assume that the light is polarised in the z-direction, i.e. $\mathbf{E} = E_0 \hat{e}_z$. When the wavelength of the light is large, the light oscillates very slowly, hence $\frac{\partial B}{\partial t} \approx 0$. There exists an electrostatic potential $\Phi(\omega, \mathbf{R})$, which satisfies

$$\nabla \Phi(\omega, \mathbf{R}) = \mathbf{E}. \tag{2.22}$$

We further assume that there is no free charge inside the system, i.e. $\rho(\mathbf{R}) = 0$. Hence, equation for Φ is given by

$$\nabla \cdot (\epsilon \nabla \Phi(\omega, \mathbf{R})) = 0. \tag{2.23}$$

We further require that the far-field potential should be equal to the incident field, i.e.

$$\lim_{|\mathbf{R}| \to \infty} \Phi(\omega, \mathbf{R}) = E_0 z = \Phi_{ext}(\mathbf{R}) \tag{2.24}$$

For a spherical nanoparticle, an analytical solution to equation 2.23 exists. Inside the nanoparticle. It is given by

$$\Phi(\omega, \mathbf{R}) = -E_0 \frac{3\epsilon_m z}{\epsilon(\omega) - 2\epsilon_m}, \tag{2.25}$$

where $\epsilon(\omega)$ is the dielectric constant inside the surrounding, and ϵ_m is the dielectric constant inside the medium. For most other shapes, an analytical solution to the equation 2.23 does not exist; we have to solve this equation numerically.

2.3.3 Perturbation in Second Quantisation

The effect of $\hat{\Phi}(\omega)$ written in the basis of atomic orbital is given by

$$\langle \mathbf{R}\alpha | \hat{\Phi}(\omega) | \mathbf{R}'\beta \rangle = \delta_{\mathbf{R}\mathbf{R}'}(\Phi(\mathbf{R};\omega) + d_{ij}\delta_{ij}), \tag{2.26}$$

The first term on the right-hand side arises because the atomic orbital is highly localised. The overlap of the neighbouring atomic orbitals under the perturbation is negligible. However, the perturbation causes transitions between different atomic orbitals. This is defined as the transition dipole matrix element $d_{\alpha\beta}$. [94] For a spherical nanoparticle,

$$d_{\alpha\beta}(\omega) = -E_0 \frac{3\epsilon_m}{\epsilon(\omega) - 2\epsilon_m} \langle \alpha\mathbf{R} | \hat{z} | \beta\mathbf{R} \rangle = -E_0 \frac{3\epsilon_m}{\epsilon(\omega) - 2\epsilon_m} \tau_{\alpha\beta}. \tag{2.27}$$

We calculate the intra-atomic matrix element $\tau_{\alpha\beta} = \langle \alpha\mathbf{R} | \hat{z} | \beta\mathbf{R} \rangle$ using ab initio density-functional theory for isolated atoms as implemented in the electronic structure program FHI-aims [95]. *These intra-atomic matrix element calculations were done by Mattias Kahk.* In these calculations, the Perdew-Burke-Ernzerhof (PBE) exchange-correlation functional [79] was used. Non-spin-polarised calculations were performed in all cases, resulting in a (n–1)d10 ns1 valence electron configuration for Cu, Ag, and Au. Scalar relativistic effects were included via the atomic ZORA formalism, and the FHI-aims default "tight" numerical basis sets were employed [95, 96]. In order to ensure that the calculated Kohn-Sham orbitals and the corresponding matrix elements match the canonical atomic orbital basis functions used in the tight binding calculations, a small external potential that lifts the degeneracies of the metal d- and p-orbitals was introduced in the DFT calculations. It was verified that the external potential did not affect the energies of the Kohn-Sham eigenstates by more than 0.01 eV. The non-vanishing matrix elements are shown in Table 2.1.

Table 2.1: Non-vanishing intra-atomic dipole matrix elements obtained from first-principles calculations, see text.

α	β	$\tau_{\alpha,\beta}$ (10^{-2} nm)		
		Ag	Au	Cu
d_{zx}	p_x	2.73	3.27	2.31
d_{yz}	p_z	2.73	3.27	2.31
d_{z^2}	p_z	3.15	3.75	2.63
s	p_z	9.36	8.95	8.55

For more complicated shapes, there is no analytical form of quasi-static potential. In such cases, we assume it is 0.

2.4 Finite-element Method

2.4.1 Weak Formulation

Solving a partial differentiation problem involves finding a potential that satisfies equation 2.23 for all points in the 3-dimensional space. This is impossible to do computationally. To do this, we have to reformulate the Laplace equation in another way.[97, 98, 99] Consider multiplying equation 2.23 with a test function $\nu(\mathbf{R})$ and integrate over all the domains Ω

$$\int_{\Omega} \nu(\mathbf{R}) \nabla \cdot (\epsilon(\mathbf{R};\omega)\nabla\Phi(\mathbf{R}))dV = 0, \tag{2.28}$$

where $\epsilon(\mathbf{R};\omega)$ is the frequency-dependent dielectric constant of the material at point $\mathbf{R}$. Using Green's identities, we get

$$\begin{aligned}\int_{V} \nu(\mathbf{R}) \nabla \cdot (\epsilon(\mathbf{R};\omega)\nabla\Phi(\mathbf{R}))dV + \int_{V} (\nabla\nu(\mathbf{R})) \cdot (\epsilon(\mathbf{R};\omega)\nabla\Phi(\mathbf{R}))dV \\ = \oint_{S} \nu(\epsilon(\mathbf{R};\omega)\nabla\Phi(\mathbf{R})) \cdot d\mathbf{S}\end{aligned} \tag{2.29}$$

for all test function $\nu(\mathbf{R})$. In addition, to fulfil the far-field condition in equation 2.24, we surround the nanoparticle with a large cube, and we set $\Phi(\mathbf{R}) = \Phi_{ext}(\mathbf{R})$ on the surface of the cube.

2.4.2 Shape Functions

To mesh the system, we use a collection of tetrahedra. This allows us to mesh finer in some regions and coarser in others. We define the shape function to be

$$\varphi_i(\mathbf{R}) = 1 \quad \text{if } \mathbf{R} = \mathbf{P}_i. \tag{2.30}$$

It can be defined in intervals (1D), triangles (2d) or tetrahedra (3D) domains. The shape function decays linearly to 0 at the neighbouring points and has a zero value at other domains (the point is not one of the corners of the domain). The 1D and 2D shape function was plotted in Figure 2.3. In 3-dimensions, if a point $\mathbf{R}$ is inside the tetrahedron $\mathbf{P}_0\mathbf{P}_1\mathbf{P}_2\mathbf{P}_3$, the shape function φ_0 is given by

$$\varphi_0 = 1 - \zeta_1 - \zeta_2 - \zeta_3, \tag{2.31}$$

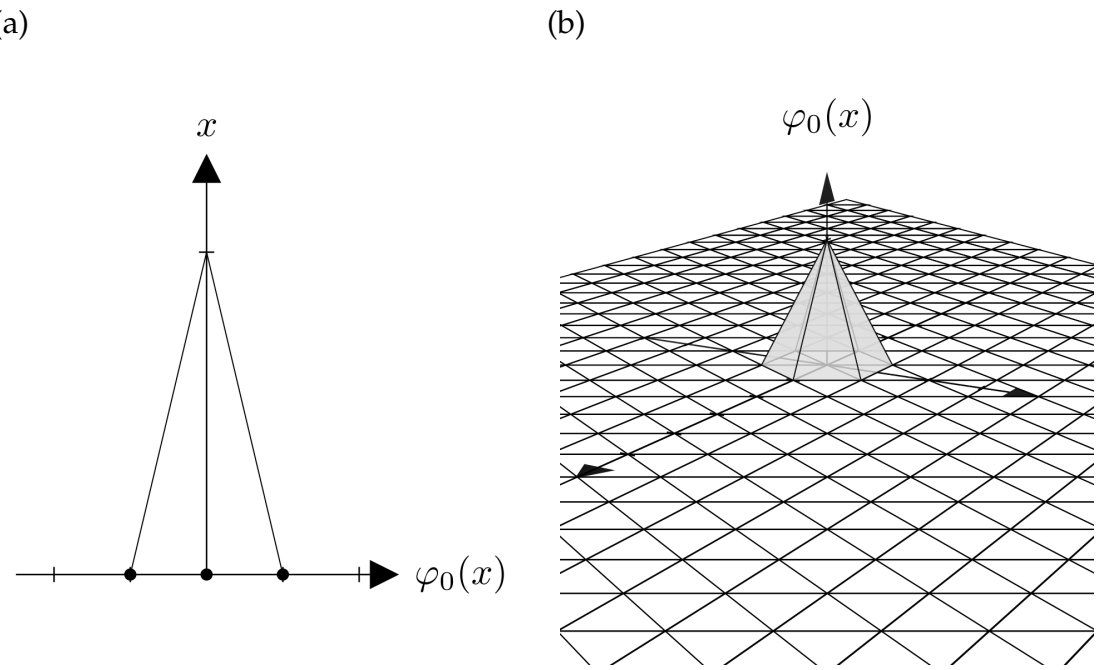

Figure 2.3: Schematic illustration of a (a) 1D shape function, (b) 2D shape function for the point in the origin $\varphi_0(\mathbf{R})$

where ζ_1, ζ_2, ζ_3 is the extent to which the point is close to $\mathbf{P}_1$, $\mathbf{P}_2$ or $\mathbf{P}_3$, respectively. They can be found by solving the following equation

$$\mathbf{R} = (1 - \zeta_1 - \zeta_2 - \zeta_3)\mathbf{P}_0 + \zeta_1\mathbf{P}_1 + \zeta_2\mathbf{P}_2 + \zeta_3\mathbf{P}_3 \tag{2.32}$$

The color plot of φ_0 on the surface of $\mathbf{P}_0\mathbf{P}_1\mathbf{P}_2\mathbf{P}_3$ is shown in figure 2.4. Note that if $\mathbf{R}$ is inside any tetrahedron that has $\mathbf{P}_0$ as one of its vertices, then it has a non-zero $\varphi_0(\mathbf{R})$. Based on the shape function, we can approximate Φ as the linear superposition of shape functions,

$$\Phi(\mathbf{R}) \approx \sum_i \xi_i \varphi_i(\mathbf{R}). \tag{2.33}$$

Similarly, we can approximate

$$\nu(\mathbf{R}) \approx \sum_j \eta_j \varphi_j(\mathbf{R}). \tag{2.34}$$

Equation 2.29 should be valid for all points inside the cube and valid for all chosen values of ", and the point at the surface of the cube is governed by equation 2.24, to satisfy both conditions. Suppose we have N interior points and M boundary

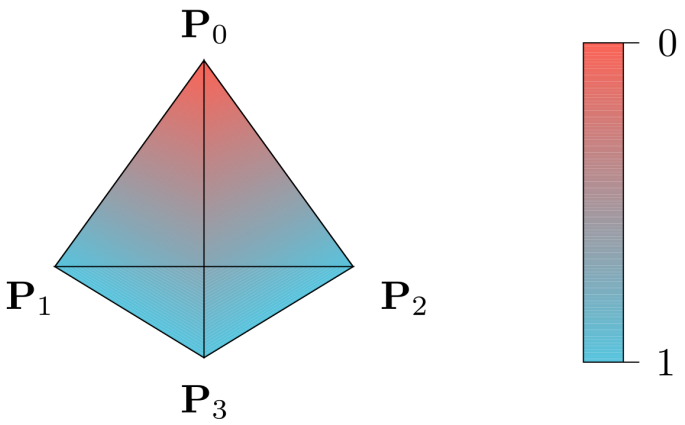

Figure 2.4: Color plot of $\varphi_0(\mathbf{R})$ on the surface of tetrahedra $\mathbf{P}_0\mathbf{P}_1\mathbf{P}_2\mathbf{P}_3$.

points,

$$\xi = \begin{pmatrix} \xi_{int} \\ \xi_{bd} \end{pmatrix}, \tag{2.35}$$

where ξ_{int} is N-dimensional vector corresponding to the interior points, and ξ_{bc} is M dimensional vectors. The coefficient for the boundary shape functions is fixed. The value of $\chi_{bd,i}$ can be obtained by

$$\xi_{bd,i} = \Phi_{ext}(\mathbf{R}_i) \tag{2.36}$$

and since in the interior, $\nabla \cdot (\epsilon \nabla \Phi(\mathbf{R}))$ should vanish everywhere, in order for equation 2.29 to be valid for all test functions in the interior,

$$\left[\underline{\underline{\chi}}_{int,int}, \underline{\underline{\chi}}_{int,bd}\right] \cdot \begin{pmatrix} \xi_{int} \\ \xi_{bd} \end{pmatrix} = \mathbf{0}, \tag{2.37}$$

or equivalently,

$$\underline{\underline{\chi}}_{int,int} \cdot \xi_{int} = -\underline{\underline{\chi}}_{int,bd} \cdot \xi_{bd}, \tag{2.38}$$

where χ is the overlap of the gradient of the i^{th} shape function with the gradient of the neighbouring shape function. It can be determined easily by

$$\chi_{i,j} = \int_V (\nabla \varphi_i(\mathbf{R})) \cdot (\epsilon_j \nabla \varphi_j(\mathbf{R})) dV. \tag{2.39}$$

$\underline{\underline{\chi}}_{int,int}$ is a $N \times N$ matrix representing the integral between interior shape function and interior shape function, $\underline{\underline{\chi}}_{int,bd}$ is a $N \times M$ matrix, representing the integral between interior shape function and boundary shape function. [100, 101] Once the

coefficient of the shape function is determined, we can interpolate the arbitrary atomic position in the cube by substituting ξ into equation 2.33.

2.4.3 Solving the Quasi-static Potential in COMSOL

Solving equation 2.38-2.39 requires advanced knowledge of mathematics, algorithms and software engineering. For example, it requires developing a 3-D platform to design nanoparticles. Apart from that, one needs to do a lot of research on how to mesh the nanoparticle and the surroundings to reflect the physics of the system. In addition, most systems require 100,000-1,000,000 shape functions to converge the calculation, so one needs to put a lot of effort into making the code scalable. These bottlenecks make developing such a finite-element solver in a PhD project impossible. Instead, we chose the commercial software COMSOL multiphysics[102, 103, 104]. Here, we briefly outline the essential steps to solve quasi-static problems using COMSOL Multiphysics.

1. Use the electrostatic module in COMSOL, select the 3D electrostatics module, and select the stationary study.
2. Design the nanoparticle shape in COMSOL.
3. Surround the nanoparticle shape with a large cube.
4. Set the dielectric constant to ϵ inside the nanoparticle. We use experimental bulk dielectric functions from reference [105]. For the dielectric region (in other words, inside the big cube), the dielectric constant was set to ϵ_m.
5. Mesh the system using tetrahedra.
6. Set the Cube value to $\Phi_{ext}(\mathbf{R}) = E_0 z$, here we use $E_0 = 8.7 \times 10^5$ V/m corresponding to an illumination intensity of 1 mW/μm^2[3].
7. Run the computation. Note that convergence is hard to achieve near the plasmonic resonance frequency, so we used the generalised minimal residual method [106] to solve the linear system of equations.
8. Input the location of atoms, COMSOL can read the locations using text file.
9. Export the output as a text file. The exported text file can be loaded using any programming language for further processing.

The process of discretising a polyhedron into a tetrahedron inside COMSOL Multiphysics is shown in Figure 2.5

[3] Note that bulk dielectric constant may become unreliable for very small nanoparticles.

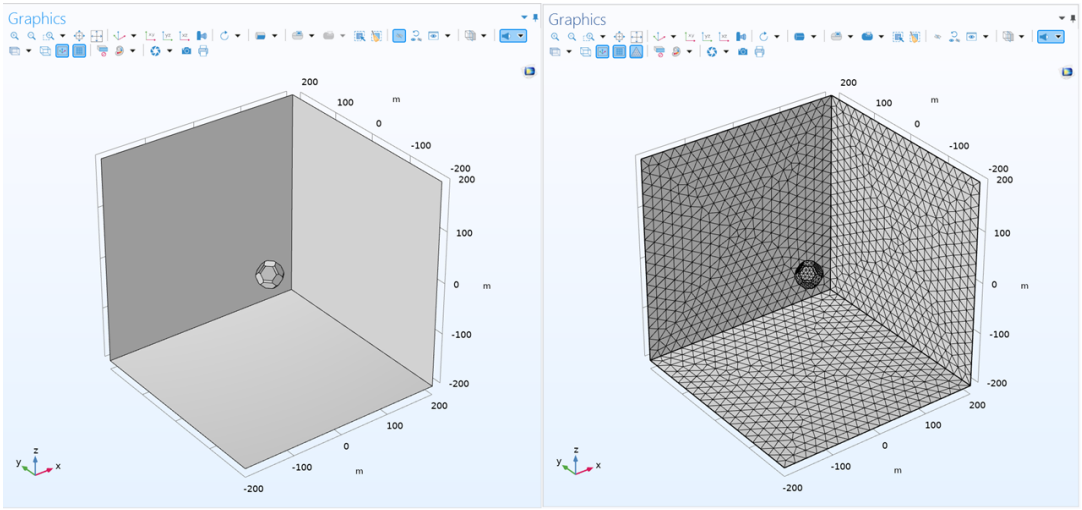

Figure 2.5: Schematic of modelling a polyhedron using COMSOL multiphysics.

2.5 The Kernel Polynomial Method

Solving equation 2.16-2.17 requires diagonalising the Hamiltonian and finding $|i\rangle$, $|f\rangle$; this makes the algorithm cubic scaling with the number of atoms. When the number of atoms exceeds 10,000, it is almost impossible to diagonalise the Hamiltonian. Nanoparticles relevant to plasmonics experiments often contain on the order of 1,000,000 atoms. To model such big nanoparticles, we need the algorithm to have linear scaling with the number of atoms.

Some researchers have exploited the sparse structure of the Hamiltonian, and they attempted to expand the spectral operator $\delta(\hat{H} - E)$ in terms of the power series of $\hat{H}$. Using this method, they successfully calculated some spectral properties of materials, such as density of states and electrical conductivity, with linear scaling complexity. However, before this project, nobody had attempted to calculate plasmonic properties using spectral methods, so we needed to develop our own linear scaling algorithm.

In this section, we are going to describe the building blocks of the Kernel Polynomial Method, in particular, the sparse matrix, the analytic functions of matrices, the Chebyshev polynomial and the spectral operator. We will then use these building blocks to derive our own linear scaling algorithm to evaluate equations 2.16-2.17.

2.5.1 Sparse Matrix

A sparse matrix[107](as illustrated in figure 2.6) is a matrix in which most entries are zero. To store these matrices, instead of storing all the entries, one can store the non-zero entries only, i.e. we store the non-zero $H_{i,j}$ and their indices i and

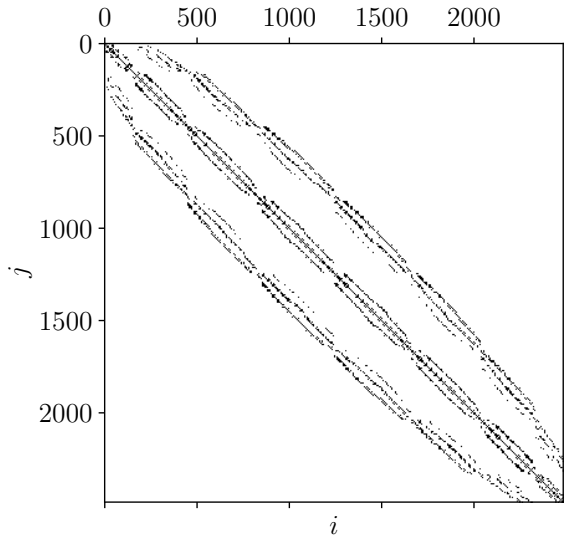

Figure 2.6: Schematic Illustration of a sparse matrix corresponding to the Hamiltonian of Au_{249} nanoparticle, the non-zero elements are represented by a black square in the corresponding i-j entry.

j. When doing matrix-vector or matrix-matrix products with sparse matrices, this data structure avoids a lot of unnecessary floating-point operations. In a Hamiltonian that was derived from fitting the Slater-Koster parameters, only nearest-neighbouring atoms have non-zero hopping values. This implies the number of non-zero matrix elements is fixed in each row of the Hamiltonian matrix. The data size of the sparse matrix thus scales linearly with the number of atoms. More importantly, consider the matrix-vector product $\langle i|\,\hat{H}\,|r\rangle$:

$$\langle i|\,\hat{H}\,|r\rangle = \sum_j H_{i,j} r_j. \tag{2.40}$$

The number of floating-point operations needed is fixed for each component i. Thus, the matrix-vector product scales linearly with the number of atoms.

2.5.2 Analytic Function of Matrices

When solving differential equations, researchers found that if analytical functions, such as e^x, can be generalised to take matrices as an argument [108, 109, 110], then the problem can be simplified significantly. A matrix can be added, subtracted, or multiplied with another matrix, and it can also be multiplied by a scalar. [111, 112] We know that we can use Tayler's expansion to expand analytic functions. This implies that we can evaluate the function of a matrix by substituting the arguments inside the Taylor's expansion [113] with Matrices. In particular, if $f(x)$ is analytic

at 0, it can be expanded as

$$f(x) = f(0) + f'(0)x + \frac{f''(0)x^2}{2!} + \cdots, \tag{2.41}$$

then $f(\hat{H})$ can be expanded as

$$f(H) = f(0) + f'(0)\hat{H} + \frac{f''(0)\hat{H}^2}{2!} + \cdots. \tag{2.42}$$

Note that if x exceeds the radius of convergence of f, then equation 2.41 is no longer valid. Similarly, if any eigenvalue of $\hat{H}$ exceeds the radius of convergence of f, then equation 2.42 will diverge.

Another way of defining the function of matrices is by diagonalisation. Suppose $|\psi_i\rangle$ is the i^{th} eigenvector of $\hat{H}$, with eigenvalue E_i, then it must also be an eigenvector of $f(\hat{H})$, with

$$f(\hat{H})\,|\psi_i\rangle = f(E_i)\,|\psi_i\rangle\,. \tag{2.43}$$

In other words, if we find $C = (|E_0\rangle, \cdots, |E_{n-1}\rangle)$ that diagonalise the Hamiltonian

$$C^\dagger \hat{H} C = \begin{pmatrix} E_0 & 0 & \cdots & 0 & 0 \\ 0 & E_1 & \ddots & \ddots & 0 \\ \vdots & \ddots & \ddots & \ddots & \vdots \\ 0 & \ddots & \ddots & E_{n-2} & 0 \\ 0 & 0 & \cdots & 0 & E_{n-1} \end{pmatrix}, \tag{2.44}$$

then $f(\hat{H})$ can be evaluated as

$$f(\hat{H}) = C \cdot \begin{pmatrix} f(E_0) & 0 & \cdots & 0 & 0 \\ 0 & f(E_1) & \ddots & \ddots & 0 \\ \vdots & \ddots & \ddots & \ddots & \vdots \\ 0 & \ddots & \ddots & f(E_{n-2}) & 0 \\ 0 & 0 & \cdots & 0 & f(E_{n-1}) \end{pmatrix} \cdot C^\dagger \tag{2.45}$$

2.5.3 Spectral Operator

The spectral operator is defined as $\delta(E - \hat{H})$. It contains a lot of important information about the physical properties of the materials. [114, 115]

Consider the case when $E \to E_0$. Using equation 2.45, we have

$$\lim_{E\to E_0} \delta(E-\hat{H}) = C \cdot \begin{pmatrix} \delta(E-E_0) & 0 & \cdots & 0 & 0 \\ 0 & 0 & \ddots & \ddots & 0 \\ \vdots & \ddots & \ddots & \ddots & \vdots \\ 0 & \ddots & \ddots & 0 & 0 \\ 0 & 0 & \cdots & 0 & 0 \end{pmatrix} \cdot C^\dagger$$
$$= |E_0\rangle \langle E_0| \, \delta(E-E_0)$$

We get the information about E_0, together with a Dirac-delta function. In other words, we can use the spectral operator to get information about the eigenstates near E.

We can also consider the trace of the spectral operator:

$$\mathrm{Tr}(\delta(E-\hat{H})) = \mathrm{Tr}\left(C \cdot \begin{pmatrix} \delta(E-E_0) & 0 & \cdots & 0 & 0 \\ 0 & \delta(E-E_1) & \ddots & \ddots & 0 \\ \vdots & \ddots & \ddots & \ddots & \vdots \\ 0 & \ddots & \ddots & \delta(E-E_{n-2}) & 0 \\ 0 & 0 & \cdots & 0 & \delta(E-E_{n-1}) \end{pmatrix} \cdot C^\dagger \right), \quad (2.46)$$

We can add a resolution of identity $C^\dagger C = 1$ into the expression, and we get

$$\mathrm{Tr}(\delta(E-\hat{H})) = \mathrm{Tr}\left(C \cdot \begin{pmatrix} \delta(E-E_0) & 0 & \cdots & 0 & 0 \\ 0 & \delta(E-E_1) & \ddots & \ddots & 0 \\ \vdots & \ddots & \ddots & \ddots & \vdots \\ 0 & \ddots & \ddots & \delta(E-E_{n-2}) & 0 \\ 0 & 0 & \cdots & 0 & \delta(E-E_{n-1}) \end{pmatrix} \cdot C^\dagger \right)$$
$$= \mathrm{Tr}\left(\underbrace{C^\dagger C}_{=1} \cdot \left(\begin{pmatrix} \delta(E-E_0) & 0 & \cdots & 0 & 0 \\ 0 & \delta(E-E_1) & \ddots & \ddots & 0 \\ \vdots & \ddots & \ddots & \ddots & \vdots \\ 0 & \ddots & \ddots & \delta(E-E_{n-2}) & 0 \\ 0 & 0 & \cdots & 0 & \delta(E-E_{n-1}) \end{pmatrix} \right) \right)$$
$$= \sum_{i=0}^{n-1} \delta(E-E_i).$$

This is the density of states or $D(E)$.

$$D(E) = \mathrm{Tr}\left(\delta(E-\hat{H})\right). \quad (2.47)$$

2.5.4 Chebyshev Polynomial

Chebyshev polynomials[116, 117] are a set of polynomials that form a complete basis set in the range of $[-1, 1]$. They can be defined using the three-term recurrence

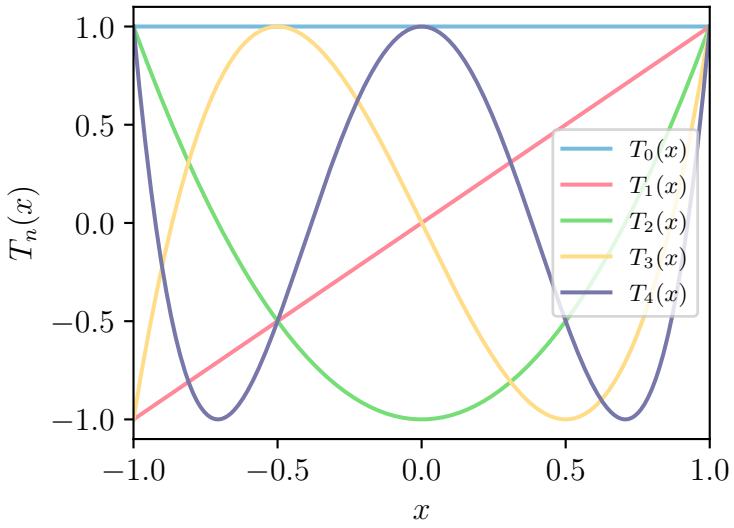

Figure 2.7: Schemetic illustration of $T_0(x)$ to $T_4(x)$.

relationship:

$$T_0(x) = 1, \tag{2.48}$$

$$T_1(x) = x, \tag{2.49}$$

$$T_{n+1}(x) = 2xT_n(x) - T_{n-1}(x). \tag{2.50}$$

Alternatively, one can define them as

$$T_n(x) = \cos(n \arccos(x)). \tag{2.51}$$

The first five polynomials are plotted in Figure 2.7. They are orthogonal with respect to the inner product

$$\int_{-1}^{1} \frac{T_n(x)T_m(x)}{\pi\sqrt{1-x^2}} \, dx = (1+\delta_{n0})\delta_{mn}. \tag{2.52}$$

With this orthogonality method, we can expand a function $f(x)$ as

$$f(x) = c_n \frac{T_n(x)}{\sqrt{1-x^2}}, \tag{2.53}$$

where c_n can be evaluated easily with the integral shown in equation 2.52. Researchers have also shown that the Chebyshev polynomials have good convergence properties in the interval $[-1, 1]$.

It has been proved that for any smooth function defined in $[-1, 1]$, the maximum discrepancy between the actual function and its Chebyshev polynomial is minimal

amongst all orthogonal polynomials. In addition, the Chebyshev polynomial converges exponentially (i.e. the coefficient decays exponentially) when the function being expanded is smooth. [108] However, we are expanding highly discontinuous Dirac-delta functions. Using Chebyshev Polynomials alone will lead to unphysical oscillation, which was treated later in this chapter.

2.5.5 Polynomial Expansion of the Spectral Operator

Now, we will expand the spectral operator $\delta(\hat{H}-E)$ using the Chebyshev polynomial. [118, 119, 120] Note that the Chebyshev polynomial diverges if any eigenvalue of $\hat{H}$ lies beyond the interval $[-1,1]$; the way to work around this is to rescale the Hamiltonian. We introduce the scaling parameters A and B:

$$A = \frac{E_0 + E_{n-1}}{2}, \tag{2.54}$$

$$B = \frac{E_{n-1} - E_0}{2} + \varepsilon, \tag{2.55}$$

where E_0 is the smallest eigenvalue and E_{n-1} is the largest eigenvalue. In equation 2.55, we add a small buffer ε to ensure that the eigenvalue lies inside the interval. Finding the exact value of E_0 and E_{n-1} requires diagonalising the full Hamiltonian, which is computationally expensive, but they can be estimated using a linear-scaling algorithm. [121] For example, looking at a smaller system, looking at the electronic structure of a bulk solid, etc.

We scale the energy E and the Hamiltonian H:

$$\mathcal{E} = \frac{E - A}{B} \tag{2.56}$$

$$\hat{h} = \frac{\hat{H} - A\hat{I}}{B}, \tag{2.57}$$

where $\hat{I}$ is the identity matrix.

Using equation 2.52-2.57, we found that the spectral operator can expand as

$$\delta(\hat{H} - E) = \frac{2}{B\pi(1+\delta_{n0})} \frac{T_n(\hat{h})T_n(\mathcal{E})}{\sqrt{1-\mathcal{E}^2}}. \tag{2.58}$$

We will now write the hot-carrier generation formula in terms of $\hat{h}$ and $\mathcal{E}$, but note that

$$\delta\left(b(x+a)\right) = \frac{1}{b}\delta(x+a), \tag{2.59}$$

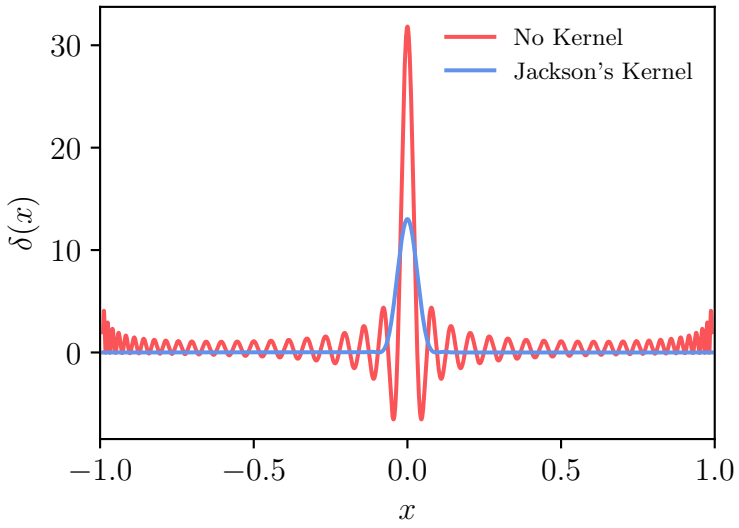

Figure 2.8: Polynomial expansion of a delta function using 100 Chebyshev polynomials.

when we convert the spectral function from units of $\mathcal{E}$ to E, we need a pre-factor of $\frac{1}{B}$ to ensure that the Dirac-delta function integrates to 1.

2.5.6 Jackson's Kernel

We now plot the Chebyshev polynomial expansion of $\delta(x)$. The delta function is highly discontinuous. If we expand it with a finite number of Chebyshev polynomials, the result will look oscillatory, as shown in figure 2.8. This phenomenon is called Gibbs oscillation. To dampen the Gibbs oscillation, we multiply each term with an additional term $J_{n,N}$. If we discard the Chebyshev polynomials of N^{th} order onwards, $J_{n,N}$ is given by

$$J_{n,N} = \frac{1}{N+1}\left((N-n+1)\cos\left(\frac{\pi n}{N+1}\right) + \sin\left(\frac{\pi n}{N+1}\right)\cot\left(\frac{\pi n}{N+1}\right)\right). \quad (2.60)$$

After multiplying each term with Jackson's Kernel[67], the Dirac-delta function becomes a Gaussian function; the broadening of this Gaussian is determined by the number of Chebyshev polynomials N used in the expansion. It is given by

$$\sigma \approx \frac{\pi}{N} \quad (2.61)$$

at the center. At -1 and +1, the broadening is approximately

$$\sigma \approx \frac{\pi}{N^{\frac{3}{2}}}. \quad (2.62)$$

2.5.7 Stochastic Trace Evaluation

Evaluating the matrix's trace is computationally expensive because a sparse matrix can gradually become dense when it is multiplied by other sparse matrices. Taking the dot product of a sparse matrix with a dense matrix scales quadratically with the number of atoms. Instead, suppose we have a quantum operator $\hat{M}$; we can evaluate the trace by multiplying it with a random vector $|k\rangle$ on the left and right-hand side of the operator. [122] I.e.

$$\mathrm{Tr}(\hat{M}) \approx \sum_{k=0}^{N_k-1} \langle k|\hat{M}|k\rangle \,, \tag{2.63}$$

where $|k\rangle$ is a random vector with its components $k_i = \langle k|i\rangle$ and $k_j = \langle k|j\rangle$ satisfies

$$\langle k_i \cdot k_i\rangle = 1 \tag{2.64}$$
$$\langle k_i \cdot k_j\rangle = 0, \tag{2.65}$$
$$\langle k_i' \cdot k_j'\rangle = 0, \tag{2.66}$$
$$\langle k_i' \cdot k_i'\rangle = 0. \tag{2.67}$$

Here, $\langle \cdots \rangle$ means taking the average of random variables inside. In this thesis, a uniform random distribution in the interval between $\left[-\sqrt{3}, \sqrt{3}\right]$ was used to estimate the trace. On average, it will reproduce the same result as tracing over the full Hilbert space. Here, N_k is the number of random vectors used in the approximation. The error is $\sim \frac{1}{\sqrt{N_k}}$. In this way, we can calculate any moment of the spectral operator using the dot product of a sparse matrix and vectors, addition/subtraction of vectors, and the vector-vector dot product. However, some literature suggests using a random complex number with unit modulus and random phase (i.e. $e^{i\theta}$, with θ uniformly distributed in $[0, 2\pi]$) or random signs(± 1) will converge faster. [123, 124, 125] By the time we found these more efficient random numbers, we had done all the calculations using uniformly distributed random variables in $[-\sqrt{3}, \sqrt{3}]$, so we were unable to use and test the more efficient distribution. But people who run KPM calculations afterwards should use this more efficient random number distribution.

2.5.8 Fermi's Golden Rule in Terms of Spectral Function

Consider one term of equation 2.16.

$$\left|\langle E_i|\,\hat{\Phi}(\omega)\,|E_f\rangle\right|^2 \delta(E_i - E_f - \hbar\omega; \gamma)\delta(E - E_f; \sigma)F(E_i)(1 - F(E_f)) \tag{2.68}$$

We can write it as an integral

$$= \int_{\mathbb{R}^2} \left| \langle E_i | \, \Phi(\hat{\omega}) \, | E_f \rangle \right|^2 \delta(\mathcal{E} - \mathcal{E}' - \hbar\omega; \gamma) \delta(E - \mathcal{E}'; \sigma) F(\mathcal{E})(1 - F(\mathcal{E}')) \\ \delta(E - E_i)\delta(E' - E_f) dE dE'. \tag{2.69}$$

Summing over all initial and final states, equation 2.16 can be expressed as

$$N_e(E, \omega) = \sum_{i,f} \int_{\mathbb{R}^2} \left| \langle E_i | \, \hat{\Phi}(\omega) \, | E_f \rangle \right|^2 \delta(E - E_i)\delta(E' - E_f) \\ \times \delta(E - E' - \hbar\omega; \gamma) \delta(E - E'; \sigma) F(E)(1 - F(E')) dE dE'. \tag{2.70}$$

Exchanging the sum and integral (which gives the same result by Fubini's theorem[126, 127]), we get

$$N_e(E, \omega) = \int_{\mathbb{R}^2} \sum_{i,f} \left| \langle E_i | \, \Phi(\hat{\omega}, r) \, | E_f \rangle \right|^2 \delta(E - E_i)\delta(E' - E_f) \\ \times \delta(E - E' - \hbar\omega; \gamma) \delta(E - E'; \sigma) F(E)(1 - F(E')) dE dE'. \tag{2.71}$$

Note that $\sum_{i,f} \left| \langle E_i | \, \Phi(\hat{\omega}) \, | E_f \rangle \right|^2 \delta(E - E_i)\delta(E' - E_f)$ is the matrix element density. It can be written as

$$\sum_{i,f} \left| \langle E_i | \, \Phi(\hat{\omega}) \, | E_f \rangle \right|^2 \delta(E - E_i)\delta(E' - E_f) = \mathrm{Tr}\left(\delta(E - \hat{H}) \Phi(\hat{\omega}) \delta(E' - \hat{H}) \Phi(\hat{\omega}) \right). \tag{2.72}$$

We arrive at our final expression of Fermi's Golden Rule in terms of spectral operators. [67, 128]

$$N_e(E, \omega) = \int_{\mathbb{R}^2} \mathrm{Tr}\left(\delta(E - \hat{H}) \hat{\Phi}(\omega) \delta(E' - \hat{H}) \hat{\Phi}(\omega) \right) \\ \delta(E - E' - \hbar\omega; \gamma) \delta(E - E'; \sigma) F(E)(1 - F(E')) dE dE'. \tag{2.73}$$

Here $\mathrm{Tr}\left(\delta(E-\hat{H})\hat{\Phi}(\omega)\delta(E'-\hat{H})\hat{\Phi}(\omega)\right)$ is the hardest quantity to calculate. It can be expanded in terms of Chebyshev moments and Chebyshev polynomials as[4]

$$\begin{aligned}
&\mathrm{Tr}\left(\delta(E-\hat{H})\hat{\Phi}(\omega)\delta(E'-\hat{H})\hat{\Phi}(\omega)\right)\\
&=\sum_{m=0}^{M-1}\sum_{n=0}^{N-1}\frac{4}{\pi^2B^2}\frac{J_{m,M}T_m(\mathcal{E})}{(1+\delta_{n0})\sqrt{1-\mathcal{E}^2}}\frac{J_{n,N}T_n(\mathcal{E}')}{(1+\delta_{m0})\sqrt{1-\mathcal{E}'^2}}\mathrm{Tr}\left(T_m(\hat{h})\hat{\Phi}(\omega)T_n(\hat{h})\hat{\Phi}(\omega)\right)\\
&=\sum_{m=0}^{M-1}\sum_{n=0}^{N-1}\frac{4}{\pi^2B^2}\frac{J_{m,M}T_m(\mathcal{E})}{(1+\delta_{n0})\sqrt{1-\mathcal{E}^2}}\frac{J_{n,N}T_n(\mathcal{E}')}{(1+\delta_{m0})\sqrt{1-\mathcal{E}'^2}}\mu_{mn},
\end{aligned} \tag{2.74}$$

where we define $\mu_{mn}=\mathrm{Tr}\left(T_m(\hat{h})\hat{\Phi}(\omega)T_n(\hat{h})\hat{\Phi}(\omega)\right)$ to be the Chebyshev moment.

With this in mind, we can write the hot-electron distribution as

$$\begin{aligned}
N_e(E,\omega)=\int_{\mathbb{R}^2}\sum_{m=0}^{M-1}\sum_{n=0}^{N-1}&\frac{4}{\pi^2B^2}\frac{J_{m,M}T_m(\mathcal{E})}{(1+\delta_{n0})\sqrt{1-\mathcal{E}^2}}\frac{J_{n,N}T_n(\mathcal{E}')}{(1+\delta_{m0})\sqrt{1-\mathcal{E}'^2}}\mu_{mn}\\
&\delta(E-E'-\hbar\omega;\gamma)\delta(E-E';\sigma)F(E)(1-F(E'))d\mathcal{E}d\mathcal{E}'.
\end{aligned} \tag{2.75}$$

By swapping the initial state E_i and the final state E_f, we can obtain an expression for the hot-hole distribution $N_h(E,\omega)$.

2.5.9 Hot-carrier Properties

Now that we have the expression for hot carrier distribution, we use it to calculate some quantities that can be measured in the experiment. The power absorbed by the nanoparticle is given by

$$P_{FG}(\omega)=\int_{-\infty}^{\infty}\left[N_e(E,\omega)+N_h(E,\omega)\right]|E|dE. \tag{2.76}$$

In this project, we also compare the power absorbed (in region i) with that computed in the quasi-static scheme given by

$$P_{QS,i}(\omega)=\frac{1}{2}\int_{V_i}|\nabla\Phi_{tot}(\omega,\mathbf{r})|^2\,\omega\Im\mathrm{m}(\epsilon(\mathbf{R};\omega))d\mathbf{r}, \tag{2.77}$$

[4] The $\frac{1}{B^2}$ factor comes from the fact that we are using different variables in the Dirac-delta function, for a detailed explanation of that, please refer to reference[129, 130]

where we integrate over the domain V_i that we are investigating. [131] The total number of electrons or holes created is given by

$$N_{e,tot}(\omega) = \int_{-\infty}^{\infty} N_e(E,\omega)dE \tag{2.78}$$

$$N_{h,tot}(\omega) = \int_{-\infty}^{\infty} N_h(E,\omega)dE \tag{2.79}$$

$$N_{tot}(\omega) = N_{e,tot}(\omega) + N_{h,tot}(\omega). \tag{2.80}$$

We found that at lower frequencies, a lot of charge carriers are produced near the Fermi level. These carriers are not energetic enough, so we define the total number of carriers that carry energy more than δ to be

$$N^{\delta}_{e,tot}(\omega) = \int_{\delta}^{\infty} N_e(E,\omega)dE, \tag{2.81}$$

$$N^{\delta}_{h,tot}(\omega) = \int_{-\infty}^{-\delta} N_h(E,\omega)dE, \tag{2.82}$$

$$N^{\delta}_{tot}(\omega) = N^{\delta}_{e,tot}(\omega) + N^{\delta}_{h,tot}(\omega). \tag{2.83}$$

In chapter 4, we do not set any energy threshold, so we define $N_{e/h,tot}(\omega)$ and $N_{tot}(\omega)$ to be the hot-carrier distribution without any energy threshold set. Many electronic devices work under solar illumination. The hot carriers generated under solar illumination are given by

$$N_{e,sol} = \int_{0}^{\infty} N_{e,tot}(\omega)S(\omega)d\omega, \tag{2.84}$$

$$N_{h,sol} = \int_{0}^{\infty} N_{h,tot}(\omega)S(\omega)d\omega, \tag{2.85}$$

$$N^{\delta}_{e,sol} = \int_{0}^{\infty} N^{\delta}_{e,tot}(\omega)S(\omega)d\omega, \tag{2.86}$$

$$N^{\delta}_{h,sol} = \int_{0}^{\infty} N^{\delta}_{h,tot}(\omega)S(\omega)d\omega. \tag{2.87}$$

Where $S(\omega)$ is the solar irradiance, it can be found in reference [132].

2.6 Convergence

Our code involves a few approximations. Firstly, we used a finite number of Chebyshev polynomials to approximate the Dirac delta function. Secondly, we used stochastic trace evaluation to evaluate $\mathrm{Tr}\left(\delta(E-\hat{H})\hat{\Phi}_{tot}(\omega)\delta(E'-\hat{H}))\hat{\Phi}^{\dagger}_{tot}(\omega)\right)$, and finally, we used finite number of tetrahedra and a finite box to solve the Poisson's equation. Without using the correct convergence parameter, it could lead

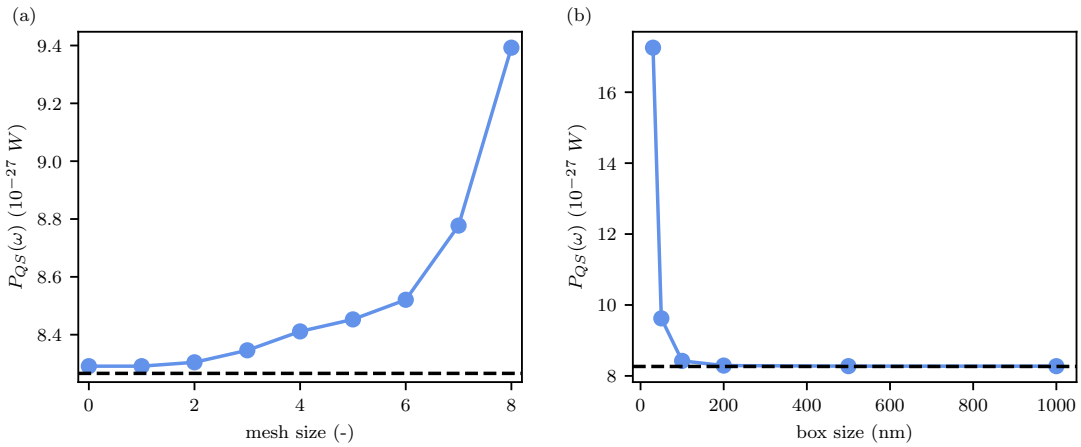

Figure 2.9: Schematic illustration of the convergence of quasi-static power with respect to the (a) mesh size, with box size fixed to 200, (b) box size, with mesh size fixed to 0 (corresponding to the 'Extremely fine' mesh).

to inaccurate results. In this section, we analyse the impact of the convergence parameters on the result.

2.6.1 Convergence of the Quasi-static Approximation

To test the convergence of the quasi-static approximation, we investigate the effect of mesh size and box size on the quasi-static potential. We compare the result for a 10 nm spherical gold nanoparticle at $\hbar\omega = 2.4$ eV (the resonance frequency). There are nine mesh sizes: "Extremely" fine, "Extra fine", "Finer", "Fine", "Normal", "Coarse", "Coarser", "Extra coarse" and "Extremely coarse". We will use the mesh size parameters 0-8 to represent them in the plotting (0 corresponds to "Extremely fine", and 9 corresponds to "Extremely coarse"). The box size also has a noticeable impact on the calculated result, as we set the box boundary to the external field $E_0 z$. We used an external field E_0 of 1 V/m.

To visualise the effect of convergence parameters on the calculated result, in figure 2.9, we plot the scattering coefficient $P_{QS}(\omega)$, described in equation 2.77, with respect to the convergence parameters.

In figure 2.9(a), we plotted the effect of mesh size on the calculation result. We can see that the mesh size up to the "Finer" setting has a negligible effect on the convergence. If we increase the mesh size further, the calculation error rises exponentially. In figure 2.9(b), we plotted the effect of box size on the error. We started with a box size of 30 nm (which corresponds to 1.5 times the diameter of the sphere) to 1000 nm (corresponding to 50 times the diameter of the sphere). It

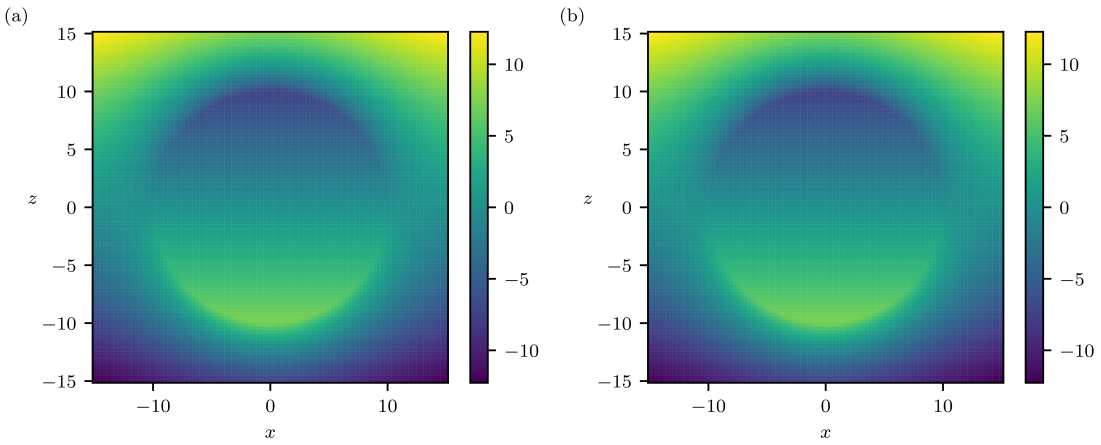

Figure 2.10: Schematic illustration of the quasi-static potential computed using COMSOL using the box size of 500 nm and mesh size of 0 (corresponding to the 'Extremely fine' mesh) versus the analytical solution.

can be seen that when the box size is less than 200 nm (corresponding to 10 times the diameter of the sphere), the error starts to grow exponentially.

To further verify the COMSOL code's correctness, in figure 2.10, we plotted the electric field near the nanoparticle in the x-z plane calculated with COMSOL versus that calculated using the analytical method described in reference [53]. It can be seen that the difference between the analytical result and the COMSOL result is negligible. We plotted the difference between the two approaches in Figure 2.11. It can be seen that the difference lies mainly outside the sphere. This is attributed to the fact that we used a linear function inside the tetrahedron to interpolate the electric potential. The difference is less than 1%. Hence, our approach of using the finite-element method to approximate quasi-static potential is valid.

2.6.2 Convergence of the Kernel Polynomial Method

In order to match the hot-carrier generation rate from the Kernel Polynomial method exactly with that computed from diagonalisation, we need to use an infinite number of Chebyshev moments and an infinite number of random vectors. This becomes impractical. We need to find a convenient point to make a cutoff with the Chebyshev moments and a finite number of random vectors. To investigate the convergence with respect to the total number of random vectors N_k and the number of Chebyshev moments N_N, we investigated a gold nanosphere containing 249 atoms; the schematics of this sphere can be found in section 3.

First, we fix $N_N = 5000$ and plot the convergence with the number of random vectors in figure 2.12. It can be seen that with a very small number of iterations

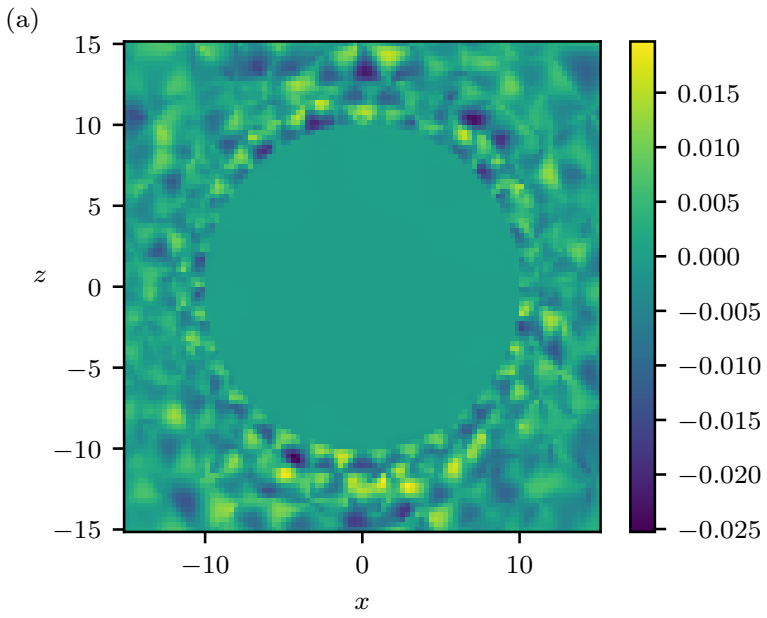

Figure 2.11: Color plot of the difference between figure 2.10(a) and figure 2.10(b)

(N_k=10), the hot-carrier generation rate is very unstable. It contains negative values, and it cannot reveal all the physically meaningful peaks that are found with a higher number of random vectors. As the number of random vectors increases to 100, most of the peaks become meaningful, but some peaks have a significantly higher magnitude; for example, the peak at -0.4 eV is higher than the peak just below the Fermi level. As the number of random vectors increases above 10000, the hot-carrier generation rate becomes stable (increasing the number of random vectors further does not have a significant impact on the values). There is a slight discrepancy with the diagonalisation result ($N_k = \infty$). This is because the diagonalisation result corresponds to using an infinite number of Chebyshev moments. The finite number of moments will broaden the peak slightly and create this discrepancy.

Next, we fix $N_k = 10000$ and vary the number of Chebyshev polynomials used. The results are plotted in Figure 2.13. It can be seen that a very small number of Chebyshev polynomials ($N_N = 50$) can lead to unphysical results. The peak (at -0.5 to -2 eV and 0.5 to 2 eV) has a much higher magnitude than other calculated results. As we increase the Chebyshev polynomial to 100, the result starts to become physical, but the resolution of the Chebyshev polynomial expansion is blurred, and it can not resolve any peaks. As the number of polynomials increases to 500 or 5000, most of the peaks become visible, but the magnitude of these peaks is slightly different from the actual result. Finally, when the number of Chebyshef polynomials reaches 10000, all the features of the matrix element density

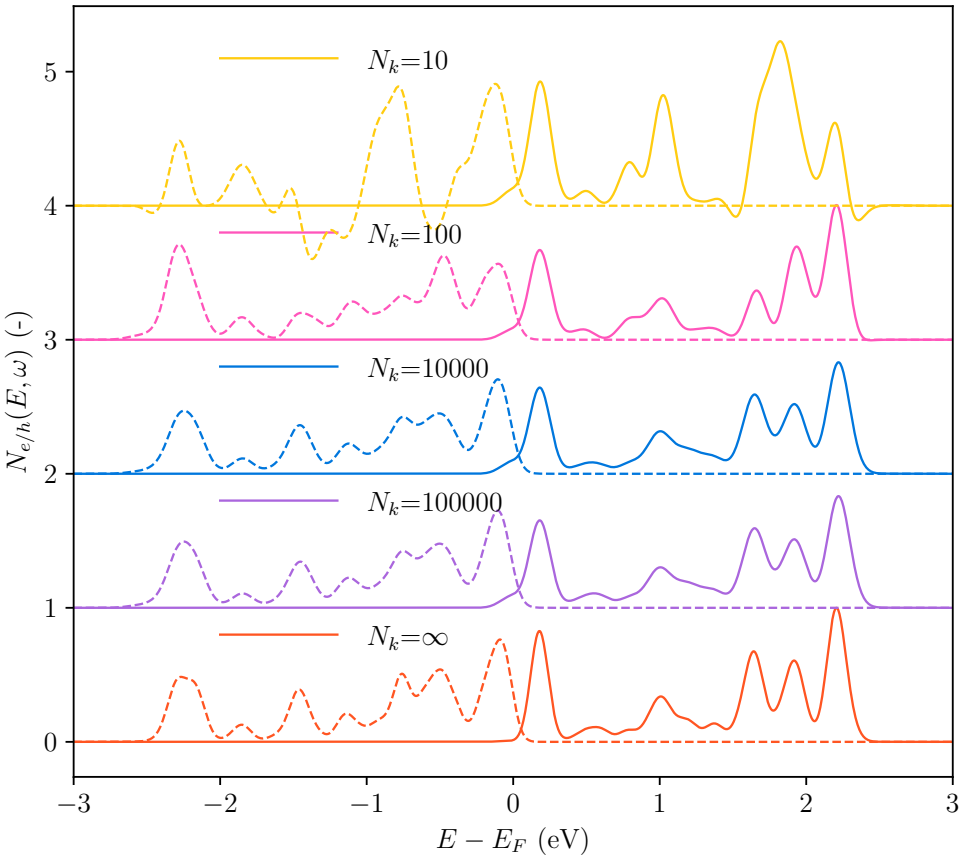

Figure 2.12: convergence of hot-carrier generation rate with the number of random vectors N_k, the solid line corresponds to the hot-electron rate, and the dashed line corresponds to the hot-hole rates. The result is normalised to the maximum value calculated using the Diagonalisation result ($N_k = \infty$), and we add an offset of 1 to each dataset to make them easy to compare.

get resolved so clearly that the result looks almost identical to that calculated by diagonalisation.

2.6.3 Comparison Between TB Method and TDDFT

Finally, we compared the hot-carrier distribution we calculated with the data computed using time-dependent density functional theory (TDDFT) calculation from Erhart's work[48]; we built a silver icosahedron nanoparticle using the method described in section 2.2. This nanoparticle has a similar number of atoms (147) to that modelled by Erhart and coworkers. [48] (This is an open access article published under a Creative Commons Attribution CC-BY License, which permits unrestricted use, distribution and reproduction in any medium,provided

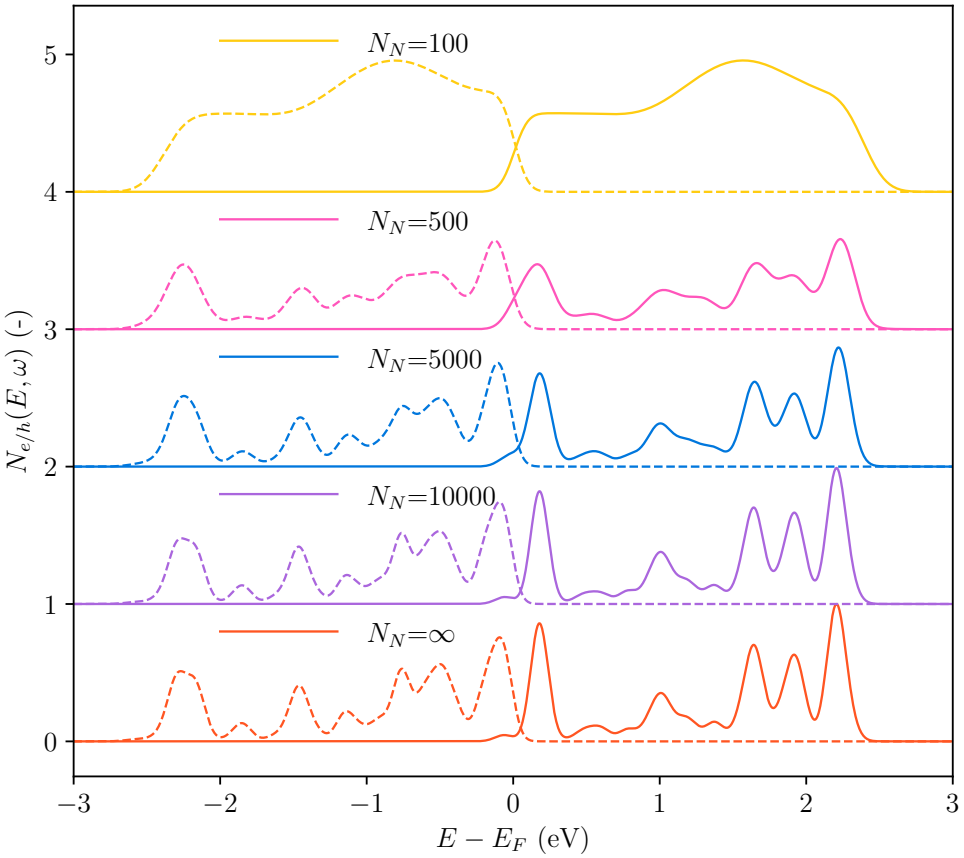

Figure 2.13: convergence of hot-carrier generation rate with the number of Chebyshev polynomials N_N, the solid line corresponds to the hot-electron rate, and the dashed line corresponds to the hot-hole rates. The result is normalised to the maximum value calculated using the Diagonalisation result ($N_k = \infty$), and we add an offset of 1 to each dataset to make them easy to compare.

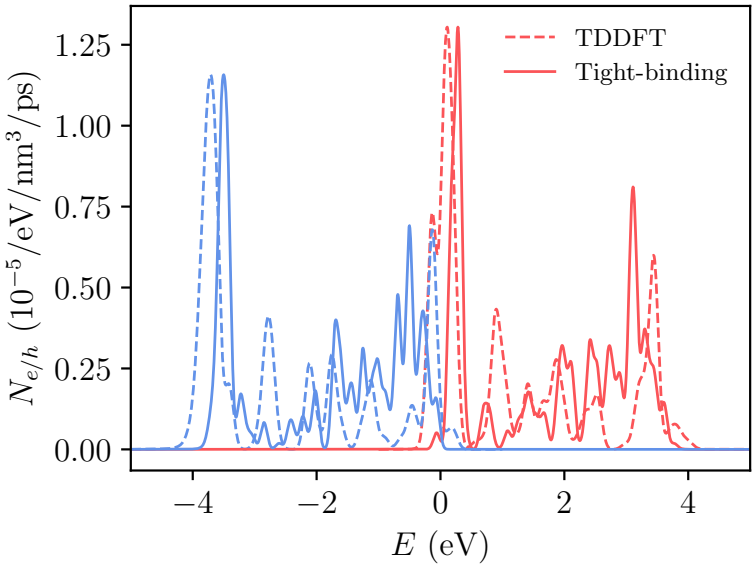

Figure 2.14: Comparison of the hot-carrier distribution computed using the tight-binding method and that computed using TDDFT from Erhart and coworkers' work. The blue line corresponds to the hot-hole generation, and the red line corresponds to the electrons. We normalised Erhart's data to the maximum value of our result.

the author and source are cited.) The results are presented in figure 2.14. It can be seen that, in general, our work matches well with the TDDFT results. Some peaks are shifted slightly and have slightly different magnitudes. This is because the lattice is slightly different, and our tight-binding parameters[59] are not fitted from GPAW, the DFT package that Erhart used. [133]

Chapter 3

Spherical Nanoparticles

3.1 Introduction

In this chapter, we use the method developed in chapter 2 to study hot-carrier generation rates in large nanoparticles of silver, gold and copper with diameters up to 30 nm, as such nanoparticles are widely used in experimental studies and hot-carrier devices. We find that hot-carrier generation rates in small nanoparticles with diameters of a few nanometers exhibit a molecule-like behaviour with discrete peaks, which evolve into a continuous distribution for larger nanoparticles. The hot-hole generation rates are characterized by a large peak at the onset of the d-bands stemming from interband d-to-sp band transitions [56]. The corresponding peak in the hot-electron generation rate is closer to the Fermi level, but its position can be controlled through the light frequency. Moreover, intraband transitions are shown to yield a second peak in the hot-hole generation rate which lies close to the Fermi level and a corresponding peak in the hot-electron rate at high energies. As the nanoparticle size increases, the interband transitions dominate increasingly over surface-enabled intraband transitions. Embedding the nanoparticle in an environment with a sufficiently large dielectric constant removes the contribution from interband hot carriers and enhances the one from intraband hot carriers. These insights from our work pave the way towards a mechanistic understanding of hot-carrier devices. For example, they enable experimentalists to design nanoparticles for specific oxidation and reduction reactions in photocatalysis.

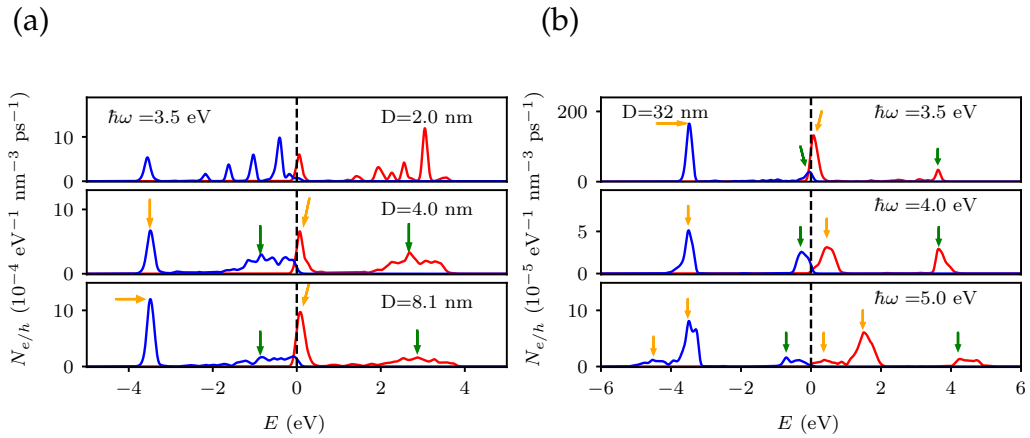

Figure 3.1: Hot-carrier generation rates for spherical silver nanoparticles. a): Dependence of the hot-hole (blue) and hot-electron (red) rates on the nanoparticle diameter D at the LSP frequency. b): Dependence of hot-carrier rates on the illumination frequency for a D = 32 nm nanoparticle. Yellow arrows indicate peaks arising from d-to-sp band transitions, and green arrows indicate peaks arising from sp-to-sp band transitions. The zero of energy is set to the Fermi level.

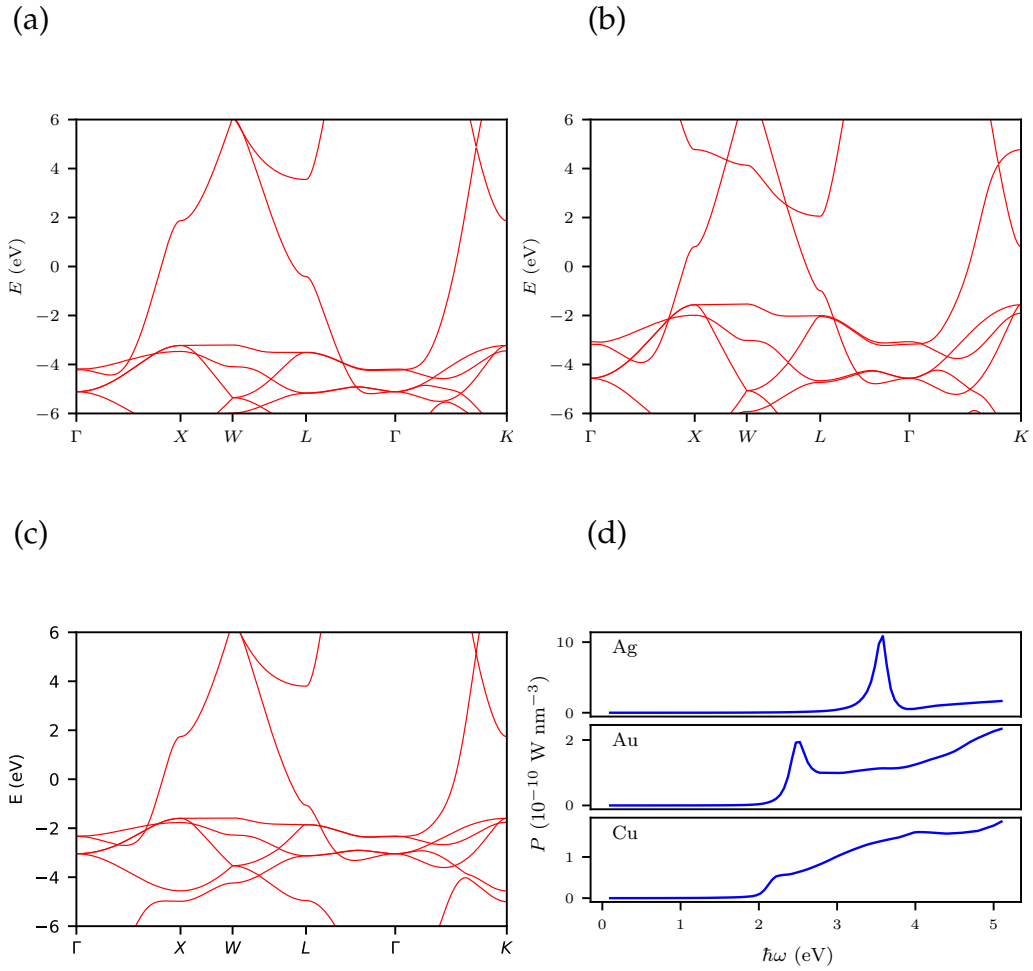

Figure 3.2: Electronic band structures of (a) silver, (b) gold and (c) copper. The zero of energy is set to the Fermi level. (d) The power (for an illumination intensity of 1 mW μm^{-2}) absorbed by the spherical nanoparticles as function of photon energy.

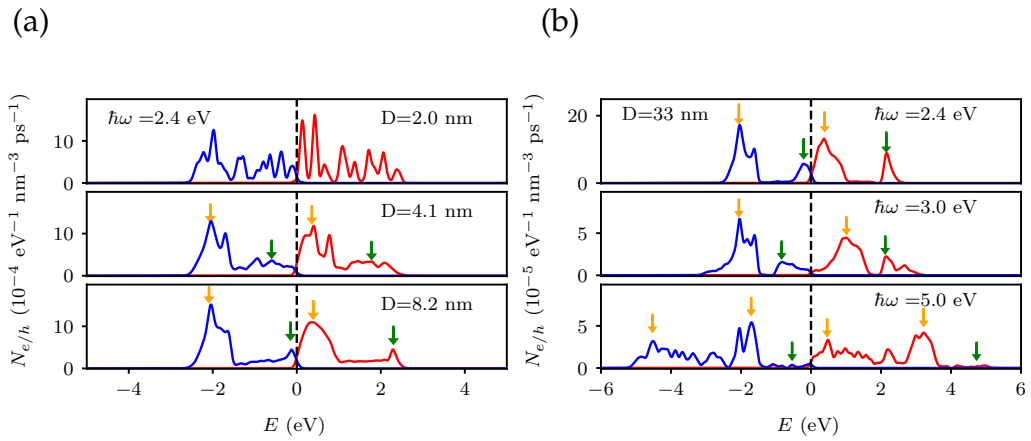

Figure 3.3: Hot-carrier generation rates for spherical gold nanoparticles. (a): Dependence of the hot-hole (blue) and hot-electron (rate) rates on the nanoparticle diameter D at the LSP frequency. (b): Dependence of hot-carrier rates on the illumination frequency for the D = 33 nm nanoparticle. Yellow arrows indicate peaks arising from d-to-sp band transitions and green arrows indicate peaks arising from sp-to-sp band transitions. The zero of energy is set to the Fermi level.

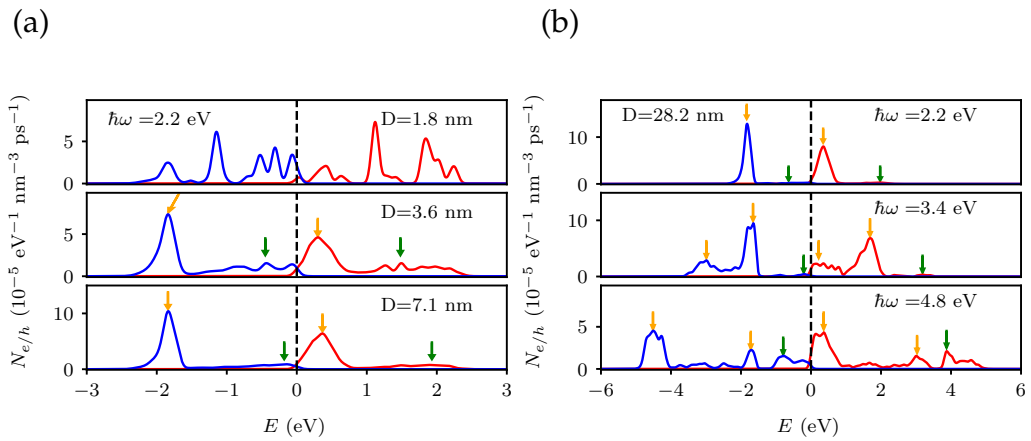

Figure 3.4: Hot-carrier generation rates for spherical copper nanoparticles. (a): Dependence of the hot-hole (blue) and hot-electron (rate) rates on the nanoparticle diameter D at the LSP frequency. (b): Dependence of hot-carrier rates on the illumination frequency for the D = 28.2 nm nanoparticle. Yellow arrows indicate peaks arising from d-to-sp band transitions and green arrows indicate peaks arising from sp-to-sp band transitions. The zero of energy is set to the Fermi level.

3.2 Hot-carrier Generation Rates.

We have calculated hot-carrier generation rates for spherical nanoparticles of Ag, Au and Cu containing up to 1,072,241 atoms (corresponding to diameters up to 32 nm (Ag), 33 nm (Au) and 28 nm (Cu)).

Figure 3.1(a) shows the evolution of the hot-electron and hot-hole generation rates in Ag nanoparticles as function of the diameter when the nanoparticle is illuminated at the LSP frequency (3.5 eV in vacuum). For the smallest nanoparticle (D=2 nm), the hot-electron and hot-hole rates exhibit a series of discrete peaks characteristic of a molecule-like behaviour. At a diameter of 4 nm, we find that the hot-electron and hot-hole rates have evolved into smooth curves. The hot-hole rate has a sharp peak near -3.5 eV (indicated by yellow arrow) and a second broader peak closer to the Fermi level (indicated by green arrow). Because of energy conservation, the hot-electron rate also exhibits a sharp peak (indicated by yellow arrow) which is shifted from the sharp peak in the hot-hole rate by the LSP energy and lies close the Fermi level. The second peak in the hot-electron rate (which corresponds to the broad peak in the hot-hole rate near the Fermi level and is indicated by a green arrow) is centered near 2.9 eV. The energy of the sharp peak (indicated by the yellow arrow) in the hot-hole rate corresponds to the onset of the flat d-bands in Ag, see Fig. 3.2. When the nanoparticle is illuminated with light at the LSP frequency, interband transitions from the d-band to the sp-band which crosses the Fermi level can be induced. The broad peaks in the hot-electron and hot-hole rates (indicated by the green arrows), on the other hand, originate from transitions from sp-band states into other sp-band states. In contrast to the d-to-sp transitions, such transitions are forbidden in the bulk material and are only enabled by the presence of the surface. As the size of the nanoparticle increases, we expect the contribution of the surface-enabled transitions to decrease in comparison to the bulk transitions. Indeed, it can be seen that the size of the broad peak is significantly reduced for a diameter of 8.1 nm in comparison to the size of the sharp peak.

Next, we study the dependence of the hot-carrier generation rates on the light frequency. Fig. 3.1(b) shows the hot-electron and hot-hole rates of a Ag nanoparticle with a diameter of 32 nm (corresponding to 1,072,241 atoms) at illumination frequencies of 3.5 eV, 4.0 eV and 5.0 eV. Again, it can be seen that the hot-electron and the hot-hole rates exhibit two peaks. The strongest peak is in the hot-hole rate at around -3.5 eV (which is indicated by a yellow arrow and corresponds to the onset of the d-bands). The corresponding peak in the hot-electron rate is shifted by the illumination frequency, i.e. it moves to higher energies as the illumination

frequency is increased. A second smaller peak in the hot-hole rate (indicated by the green arrow) occurs just below the Fermi level where the density of occupied sp-band states is highest. This peak moves to lower energies as the illumination frequency is increased. The corresponding peak in the hot-electron rate is located near 4.0 eV and moves to slightly higher energies as the light frequency is increased. These results show that hot holes are predominantly produced in the d-band (as a result of d-to-sp transitions), but also near the Fermi level. In contrast, the energy of hot electrons generated by bulk transitions can be controlled through the illumination frequency, while the energy of surface-enabled hot electrons is very high. It can also be seen that the highest number of hot carriers are produced at the LSP frequency as a consequence of the large enhancement of the field intensity. At the LSP frequency, bulk transitions are much more frequent than surface-enabled transitions. In contrast, the relative contribution of surface-enabled hot carriers increases for higher illumination frequencies.

Figure 3.3 shows the hot-carrier rates for Au nanoparticles. At the LSP frequency (2.4 eV in vacuum), the hot-carrier rates again exhibit discrete peaks for small nanoparticles, which evolve into continuous distributions as the diameter increases, see Fig. 3.3(a). The main peak in the hot-hole rate (indicated by yellow arrow) for the larger nanoparticles is located at -2.0 eV corresponding to the onset of d-bands in the material, see Fig. 3.2(b). A corresponding peak in the hot-electron rate is located just above the Fermi level (also indicated by a yellow arrow). Both rates also exhibit a second smaller peak (indicated by green arrows) caused by surface-enabled sp-to-sp transitions. This second peak is just below the Fermi level in the hot-hole rate and near +2.3 eV in the hot-electron rate.

Considering next the evolution as function of light frequency for a nanoparticle of 33 nm diameter, see Fig. 3.3(b), shows that the main peak (indicated by a yellow arrow) in the hot-hole generation rate remains at -2.0 eV while the corresponding peak in the hot-electron rate moves to higher energies. In contrast to Ag, an additional hot-hole peak emerges at lower energies (near -4.5 eV for a light frequency of 5 eV, also indicated by a yellow arrow) with a corresponding hot-electron peak just above the Fermi level. These peaks result from transitions from deeper lying d-bands to sp-bands. The hot-hole peak just below the Fermi level disappears as the light frequency increases.

After that, we consider Cu nanoparticles. In this system, the LSP peak at 2.2 eV is much less pronounced, see Figs. 3.2(c) and (d). As a consequence, the hot-carrier peaks at the LSP frequency are much lower than in Ag and Au, see Fig. 3.4(a). Similarly, to the case of Ag, we find a peak in the hot-hole rate (indicated by yellow

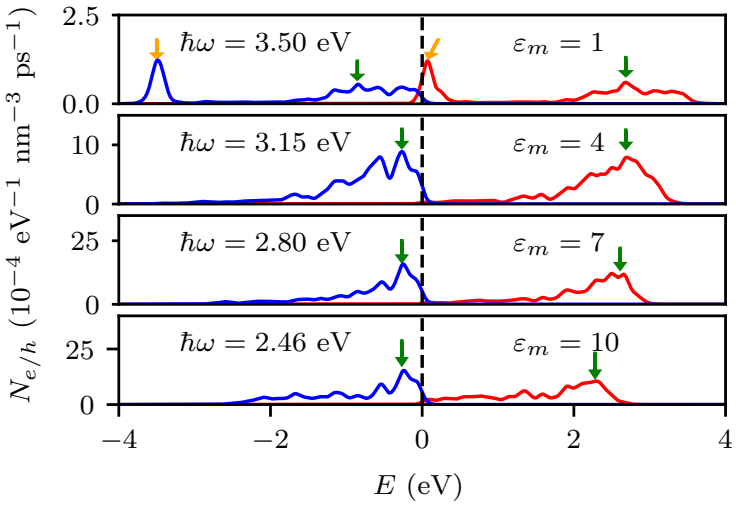

Figure 3.5: Hot-carrier distribution of a spherical silver nanoparticle with a diameter of 4 nm in various dielectric environments evaluated at the corresponding LSP frequencies. Yellow arrows indicate peaks arising from d-to-sp band transitions, and green arrows indicate peaks arising from sp-to-sp band transitions.

arrow) at -1.8 eV corresponding to bulk d-to-sp transitions with a corresponding hot-electron peak just above the Fermi level. A second smaller peak in the hot hole rate (indicated by green arrow) arising from surface-enabled sp-to-sp transition is found just below the Fermi level and a corresponding hot electron peak near 2 eV. At higher frequencies, additional peaks at lower energies (indicated by yellow arrows) emerge in the hot-hole rate as a consequence of transitions from low-lying d-states. In particular, at a light frequency of 4.8 eV the strongest peak is located at -4.5 eV and a corresponding peak in the hot-electron rate is located at +0.4 eV.

Finally, we study the dependence of the hot-carrier generation rates on the dielectric constant of the surrounding medium. Fig. 3.5 shows results for a silver nanoparticle with a diameter of 4 nm. As discussed above, in vacuum ($\epsilon_m = 1$), the hot-hole generation rate has a large peak at -3.5 eV due to interband transitions with a corresponding hot-electron peak near the Fermi level (indicated by yellow arrows). For $\epsilon_m = 4$, the LSP frequency has reduced to 3.15 eV. This is no longer sufficient to excite interband transitions and the hot-hole rate is characterized by a broad peak near the Fermi level, while the hot-hole rate exhibits a corresponding peak near 3 eV (indicated by green arrows). Interestingly, the height of the intraband peak is increased compared to the case of vacuum. This increase is caused by an increase in the matrix elements [56, 134] which are proportional to $1/\omega^2$ [56]. As the medium dielectric constant increases, the main peak of the hot-hole generation rate remains close to the Fermi level while the energy of the hot electrons is reduced. These findings demonstrate that hot-carrier generation rates can be controlled by a careful choice of the dielectric properties of the nanoparticle environment.

3.3 Summary

We have reported atomistic quantum-mechanical calculations of plasmon-induced hot-carrier generation rates in large nanoparticles containing more than one million atoms. Accessing this size regime which is relevant for practical devices is possible through the use of highly efficient spectral methods based on an expansions of the hot-carrier generation rate in terms of Chebyshev polynomials. These advances allow us to study the evolution of the hot-carrier generation rate as function of nanoparticle diameter from a molecule-like regime characterized by discrete peaks to a continuous curve for diameters exceeding 4 nm. Moreover, the relative importance of bulk d-band to sp-band transitions compared to surface-enabled sp-band to sp-band transitions increases with increasing diameter. Interband transitions give rise to a large peak in the hot-hole generation rate located at the onset of d-band states. Such holes have energies of several electron volts relative to the Fermi level. The corresponding peak in the hot-electron rate lies closer to the Fermi level, but is tunable through the illumination frequency. In contrast, intraband transitions induce holes near the Fermi level and hot electrons with energies of several electron volts. Finally, the contribution to the hot-carrier distributions arising from interband transitions can be removed by increasing the dielectric constant of the surrounding medium which also enhances the matrix elements for intraband transitions. These insights are crucial for fabricating nanoparticles to induce and optimize specific chemical reactions. They also form the starting point for studying the thermalization of hot electrons, which is the subject of future work.

Chapter 4

Bimetallic Plasmonic Catalysts

4.1 Introduction

Photocatalytic hot-carrier devices often have relatively low efficiencies [135]. A possible explanation for this is that standard plasmonic materials, such as Au and Ag, are generally not good catalysts[137]. Therefore, attempts have been made to combine plasmonic materials with catalytic materials, such as Pt, Pd or Rh, into functional nanoarchitectures. Examples of such heterostructures include Janus nanoparticles [136], core-shell systems [138, 139] or nanoparticle dimers and trimers [140]. Recently, Herran and coworkers studied different nanoarchitectures of Pd and Au, including core-shell nanoparticles and antenna-reactor systems (as shown in figure 4.1) in which a large Au nanoparticle is "decorated" with small Pd nanoparticles (or satellites), for the production of H_2 from formic acid [141]. These authors found significant enhancements in H_2 production upon illumination of the plasmo-catalyst, with the largest increase in chemical activity for antenna-reactor systems. Despite these advances, however, there is still no detailed microscopic understanding of the catalytic activity in bimetallic nanoarchitectures[142].

In this Chapter, we use the method developed in section 2 to study the enhancement of hot-carrier generation rates in a catalytic metal (Pd) induced by the presence of a plasmonic metal (Au) in different bimetallic plasmonic-catalytic nanoarchitectures. In particular, we study Au@Pd core-shell nanoparticles and antenna-reactor systems consisting of a large Au nanoparticle, which acts as an antenna and a small satellite nanoparticle. The satellite is either a spherical Pd nanoparticle or an Au@Pd core-shell nanoparticle. We compare our results to hot-carrier generation rates in spherical Pd nanoparticles. We find that the largest hot-carrier generation rates in the catalytic metal are found in antenna-reactor systems, in particular in

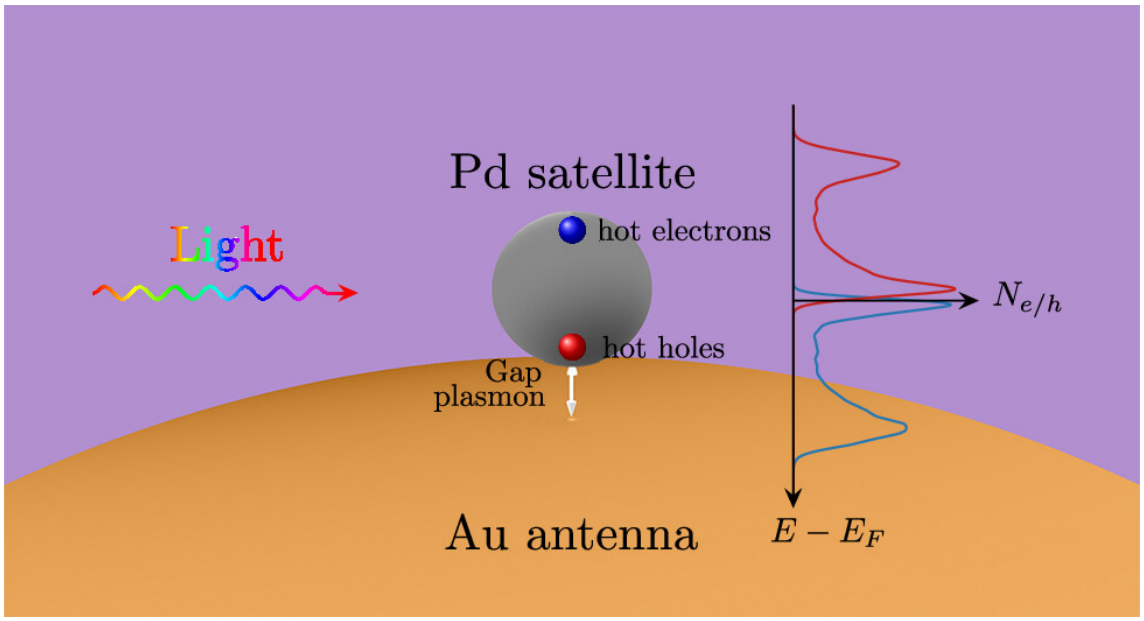

Figure 4.1: Schematic illustration of an antenna-reactor system.

those where the satellite nanoparticle is a core-shell system. This can be explained by the large enhancement of the electric field arising from the strongly confined plasmon mode associated with the gap between the antenna nanoparticle and the satellite nanoparticle. We also explore the dependence of hot-carrier generation rates on light polarization, the size of the antenna nanoparticle, and the gap between the antenna nanoparticle and the satellite. We compare our calculated hot-carrier generation rates to experimentally measured H_2 production rates [141] for different Au-Pd photocatalysts and find a strong correlation between the two. The insights resulting from our work pave the way towards a microscopic design of heterogeneous nanoarchitectures for energy conversion devices. The approach can readily be applied to other materials.

4.2 Method

Currently, there is no Tight-Binding model that models the palladium and gold spherical nanoparticles, instead, we used an approximation to work around it.

Once we determine the total potential of the full Au-Pd nanoarchitecture, we evaluate the hot-carrier generation rate in the Pd subsystem (as only the hot carriers in the Pd are catalytically active). Note that our approach does not capture charge transfer processes between the Au and the Pd, which can play an important role in core-shell nanoparticles [143, 144]. In contrast, charge transfer is not expected to be important in antenna-satellite systems because of the finite gap (caused by the presence of surfactants) between the antenna and the satellite

nanoparticle [141]. The electronic states of the Pd subsystem are obtained using the approach mentioned in section 2.

4.3 Results and Discussion

We have calculated hot-carrier generation rates in four systems, see Fig. 4.2: (a) spherical Pd nanoparticles consisting of 3589 atoms (corresponding to a diameter $D = 4.42$ nm), (b) spherical Au@Pd core-shell nanoparticles with an Au core (of diameter $D_c = 4.90$ nm) and a Pd shell (of thickness 0.40 nm containing 3740 Pd atoms), (c) an Au-Pd antenna-reactor architecture consisting of a small spherical Pd nanoparticle of the same size as in (a) which is separated by a small gap from a larger Au nanoparticle and (d) an Au-Au@Pd antenna-reactor architecture in which the small nanoparticle has a core-shell structure as in (b). The sizes of the Pd nanoparticle and of the Au@Pd core-shell nanoparticle are similar to the satellite nanoparticles used in the experiment of Herran and coworkers [141]. Note that we are only studying hot-carrier generation in the Pd subsystems of the various Au-Pd photocatalysts. As all photocatalysts contain a similar number of Pd atoms (and we further report the hot-carrier generation rate per unit volume), we are confident that a quantitative comparison of the hot-carrier generation rates of the different photocatalysts is physically meaningful.

Figure 4.3(a) shows the evolution of the hot carrier generation rate for the spherical Pd nanoparticle as a function of photon energy. Both the hot hole and the hot electron rates exhibit two peaks. The hot hole rate has a peak near the Fermi level, with the hot electron rate having a corresponding peak at $\sim \hbar\omega$ above the Fermi level. The other peak of the hot hole rate is at $\sim -\hbar\omega$, and the hot electron rate has a corresponding peak just above the Fermi level. As the photon energy is varied, the peaks near the Fermi level are pinned at their positions, but the other peaks move to higher (in the case of the hot electron rate) and lower (in the case of the hot hole rate) energies. This finding can be understood from an analysis of the electronic structure of Pd. In particular, the band structure of Pd, see Fig. 4.2(e), exhibits flat d-bands just above and below the Fermi energy. These flat bands give rise to a large density of states, which translates into a high hot carrier generation rate near the Fermi level. The positions of the other peaks are then determined by energy conservation, i.e. for each electron of energy E, a corresponding hole of energy $E - \hbar\omega$ must be created. Finally, we do not observe a dramatic enhancement of the hot-carrier rates at a particular photon energy, reflecting the absence of a strong LSP resonance in spherical Pd nanoparticles.

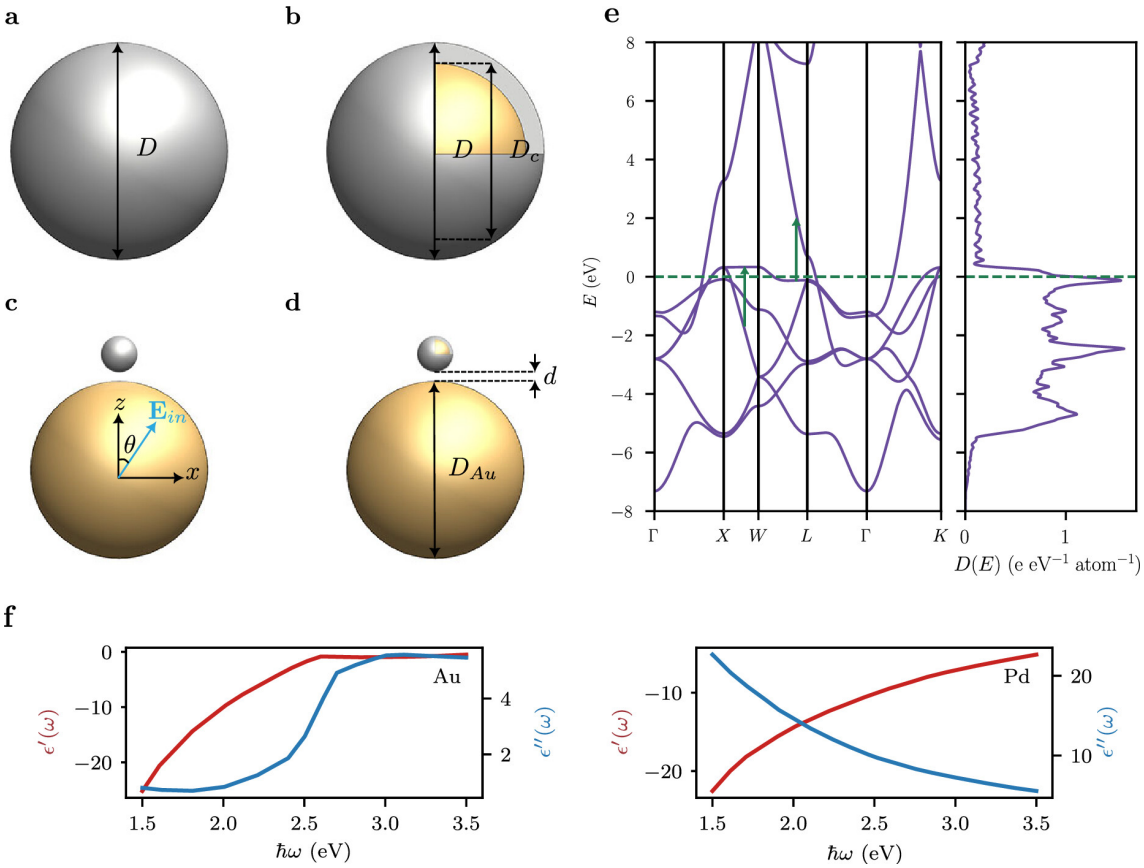

Figure 4.2: Schematic illustration of (a) a spherical Pd nanoparticle, (b) an Au@Pd core-shell nanoparticle, (c) an Au-Pd antenna-reactor system and (d) an Au-Au@Pd antenna-reactor system, (e) band structure of bulk fcc Pd, the zero of energy is set to the Fermi level (indicated by the green dashed line). Green arrows indicate interband transitions involving flat d-bands near the Fermi level. (f) Real and imaginary parts of the dielectric functions of Au and Pd. From Ref. [105]

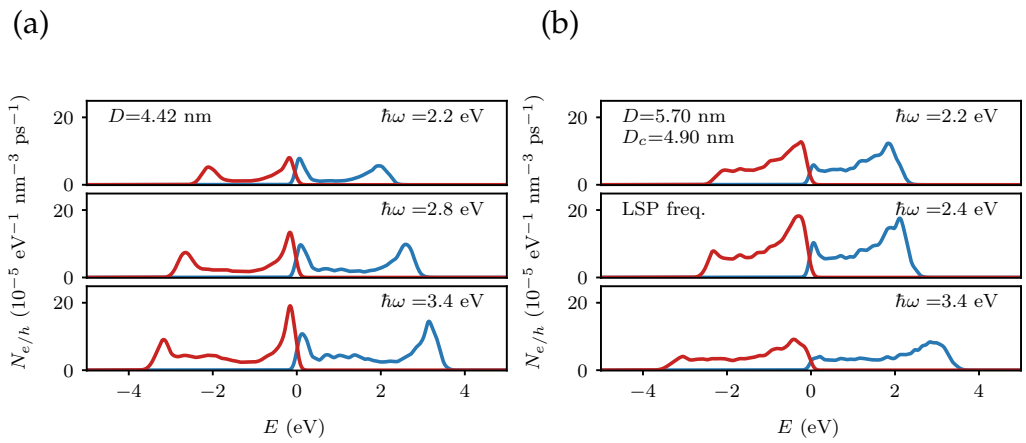

Figure 4.3: Dependence of hot-carrier generation rate on photon energy for (a) a spherical Pd nanoparticle with a diameter of $D = 4.42$ nm and (b) an Au@Pd core-shell nanoparticle with a core diameter of $D_c = 4.90$ nm and a shell thickness of 0.40 nm. Hot hole (electron) generation rates are red (blue). The zero of energy is set to the Fermi level.

Figure 4.3(b) shows the dependence of the hot carrier generation rate of an Au@Pd core-shell nanoparticle on the photon energy. Again, the rates exhibit peaks near the Fermi level. Some differences in the shapes of the hot-carrier generation rates can be observed compared to the spherical Pd nanoparticle: these are caused by the increase of the surface area of the thin Pd shell, which enhances the generation of hot carriers from intraband transitions [68]. In the core-shell system, an enhancement of the hot-carrier generation rate at a photon frequency of 2.4 eV can be observed. This energy is close to the LSP energy of a spherical Au nanoparticle. In other words, at this photon energy, the field enhancement of the Au core increases the hot-carrier generation in the Pd shell [144].

Next, we investigate hot-carrier generation in the Au-Pd antenna-reactor system. Adding the Au nanoparticle to the spherical Pd nanoparticle lifts the rotational symmetry of the Pd system. As a consequence, the hot-carrier generation rate now depends on the polarization vector of the electric field. We assume that both the centre of the Au and the centre of the Pd nanoparticle lie on the z-axis, see Fig. 4.2, and describe the electric field through its polar angle θ. Fig. 4.4(a) shows the dependence of the hot carrier rate on θ. The hot-carrier generation rate is largest when $\theta = 0°$ and then decreases as θ is increased. In particular, we find that the hot-carrier generation rate is proportional to $\cos\theta$, i.e. $N_e(\omega, E, \theta) = N_e(\omega, E, 0)\cos\theta$. When $\theta = 0$, the charge carriers in the Au nanoparticle are pushed towards the Pd nanoparticle, creating a strongly enhanced electric field. The field is further enhanced by the confinement effect of the small gap between the Au and the Pd nanoparticles, giving rise to a so-called gap plasmon [145]. We note that a large number of satellites are attached to the Au nanoparticles in the experiments of

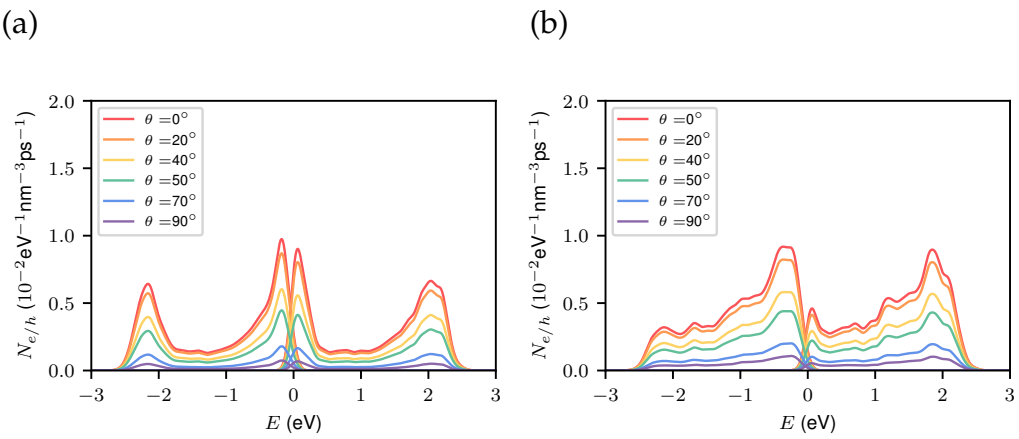

Figure 4.4: Dependence of hot-carrier generation rate on light polarization for (a) an Au-Pd antenna-reactor system with a diameter of 4.42 nm, (b) Au-Au@Pd reactor system, with a core diameter of 4.9 nm and a total diameter of 5.7 nm. The diameter of the Au nanoparticle is 49 nm. The size of the gap between the Pd and Au nanoparticles is 0.40 nm and the photon energy is is 2.28 eV for Au-Pd system and 2.20 for Au-Au@Pd system.

Herran and coworkers [141]. Also, the light used in experiments is not polarized. Therefore, the experimentally measured hot-carrier generation rate is an average over θ.

Figure 4.4 shows the same results for an Au-Au@Pd antenna-reactor system. Again, the hot-carrier generation rate of the core-shell system has a different shape than the pure Pd system, but it exhibits a similar dependence on light polarization.

Next, we study the dependence of the hot-carrier generation rate of the two antenna-reactor systems on the size of the gap d between the Au nanoparticle and the satellite, see Fig. 4.5. In practice, this parameter is determined by the size of the ligands on the surface of the nanoparticles and is difficult to control experimentally (in the experiment of Herran et al., the gap is estimated to be approximately 1 nm [141]). We find that the largest hot-carrier rates are obtained for the systems with the smallest gaps. The insets show that the total number of hot carriers decreases quickly as the gap size is increased. For example, increasing the gap from 0.49 nm to 1.6 nm reduces the total number of hot carriers by a factor of 0.38 (Au-Au@Pd) and 0.42 (Au-Pd) and further increases to d = 3.2 nm gives rise to an additional reduction by a factor of 0.58 (Au-Au@Pd) and 0.63 (Au-Pd) in the total hot carrier generation rate. This result demonstrates the importance of the confinement effect associated with the gap between the Au and the satellite particles on the strength of the electric field.

Next, we study the dependence of the Pd hot-carrier generation rate of the reactor systems on the size of the Au nanoparticle, see Fig. 4.6. We find that the hot-carrier

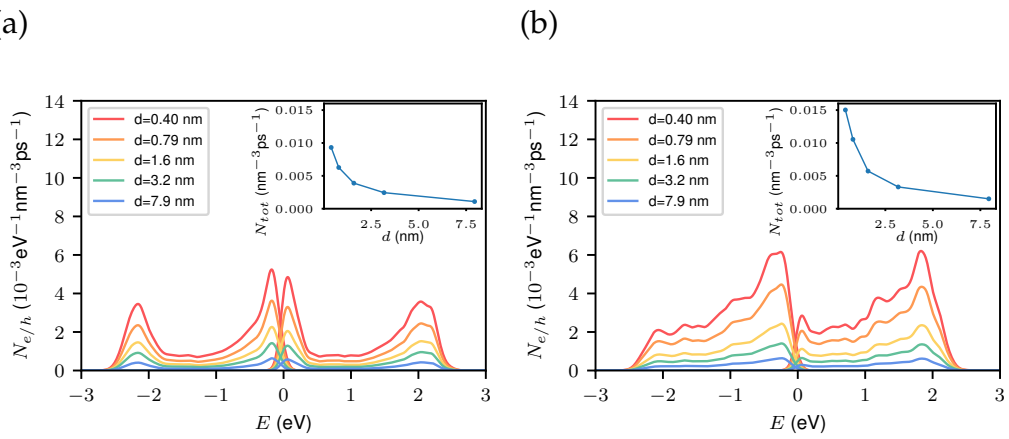

Figure 4.5: Dependence of the hot-carrier generation of Au-Pd antenna-reactor systems on the size of the gap d between the Au nanoparticle and the satellite. (a) Results for a Pd satellite. (b) Results for an Au@Pd core-shell satellite. The diameter of the Au antenna nanoparticle is 49 nm, the photon energy is 2.28 eV for the Au-Pd system and 2.20 for the Au-Au@Pd system, and the calculation is averaged over all polarization angles. The insets show the total hot-carrier generation rate

generation rate increases as the size of the Au nanoparticle increases. Increasing the Au nanoparticle size while keeping the distance between the Au nanoparticle and the satellite fixed reduces the volume available in the gap between the two nanoparticles and thus enhances confinement effects. This, in turn, leads to electric field enhancement. As the Au nanoparticle size increases, the additional reduction of the gap volume becomes smaller and smaller and only results in a small increase in hot carrier production.

Finally, we study the dependence of the hot-carrier generation rates of the reactor systems on the photon energy, see Fig. 4.7. For both systems, a dramatic enhancement of the rates is observed at a photon energy of 2.24 eV compared to the other photon energies. This photon energy is close to the LSP energy of the Au nanoparticle (note that the presence of the satellite modifies the LSP energy of the Au nanoparticle) so the increase of the hot-carrier generation rates reflects the electric field enhancement caused by the plasmon mode. The LSP acts as an optical lens which efficiently funnels energy towards the catalytic material.

We compare the total Pd hot-carrier generation rates of the four different systems (spherical Pd nanoparticle, Au@Pd core-shell nanoparticle, Au-Pd antenna-reactor system and Au-Au@Pd antenna-reactor system) in Fig. 4.8(a). It can be seen that the two antenna-reactor systems produce significantly more hot carriers in the Pd than the other two systems. In particular, a dramatic increase in the generation rate is observed near the plasmon frequency of ~ 2.2 eV. As discussed above, the large generation rates are a consequence of the gap plasmon mode, which gives rise to

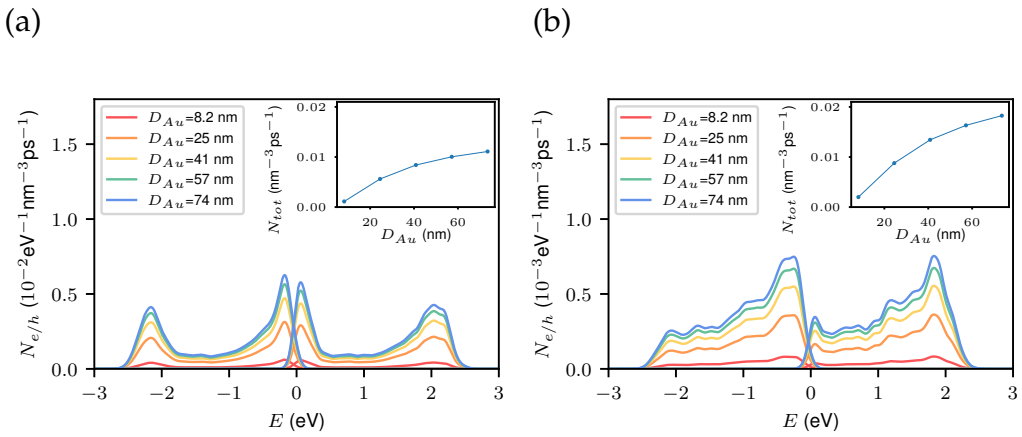

Figure 4.6: Dependence on the hot-carrier generation of Au-Pd antenna-reactor systems on the size of the Au nanoparticle. (a) Results for a Pd satellite. (b) Results for an Au@Pd core-shell satellite. The size of the gap is 0.40 nm, the photon energy is 2.28 eV for Au-Pd system and 2.20 eV for Au-Au@Pd system and the calculation was averaged over all polarization angles. The insets show the total hot-carrier generation rates.

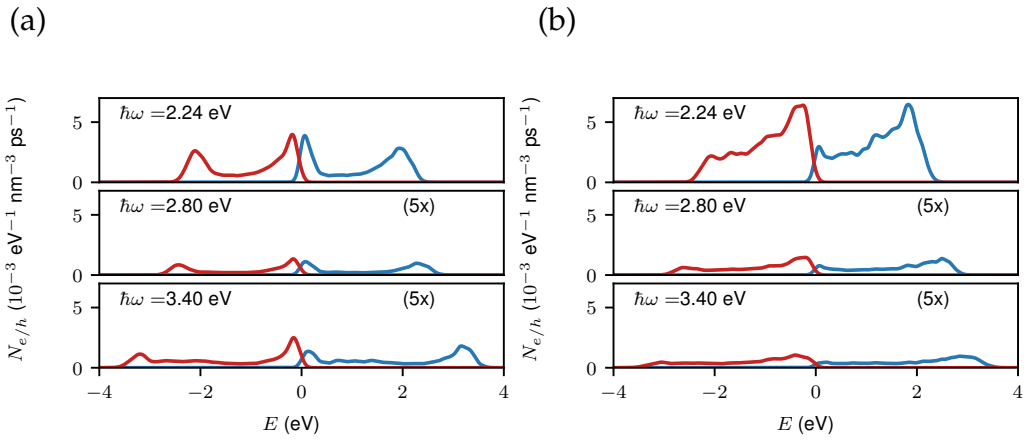

Figure 4.7: Dependence of hot-carrier generation rate on the photon energy for (a) an Au-Pd antenna-reactor system with a diameter of 4.42 nm, (b) Au-Au@Pd antenna-reactor system, with a core diameter of 4.9 nm and a total diameter of 5.7 nm. The diameter of the Au nanoparticle is 49 nm. The size of the gap between the Pd and Au nanoparticles is 0.40 nm, and the calculation is averaged over all polarisation angles. For visual aid, the hot-carrier generation rates at $\hbar\omega = 2.80$ eV and 3.40 eV were multiplied by a factor of 5.

large electric field enhancements. In the antenna-reactor system with a core-shell satellite, the electric field is more strongly confined because of the presence of the Au inside the core-shell satellite, and therefore, this system gives rise to the largest hot-carrier generation rate overall.

In their experiments, Herran and coworkers measure the increase in H_2 production from formic acid by bimetallic plasmonic catalysts upon illumination with a solar simulator (see Figure 2(a) of Ref. [141]). In Fig. 4.8(b), we show the measured difference in H_2 production in the dark and upon illumination for an Au@Pd core-shell nanoparticle, an Au-Pd antenna-satellite system and an Au-Au@Pd system. We compare this difference to the total number of hot holes N_{sol} generated by the solar spectrum $S(\omega)$ (using the Air Mass 1.5 spectrum).

In excellent agreement with the experiment, we find that the Au-Au@Pd antenna-satellite system is the best bimetallic plasmonic photocatalyst, while the Au@Pd system performs much worse. We note that the agreement between theory and experiment is somewhat worse for the Au@Pd system - this is likely a consequence of the different nanoparticle sizes used in the experiment and in our calculations and also of the neglect of charge transfer between core and shell in our model.

We note that we have not included hot-carrier relaxation effects in our calculations. Moreover, we did not include a detailed description of the interaction of the hot carriers with the reactive molecular species. Extending our formalism for modelling hot-carrier generation rates to include these effects will be the topic of future work. Despite this, the correlation between our theory and the experimental results is remarkable, as shown in Fig. 4.8(b).

4.4 Conclusion

We have studied hot-carrier generation in Au-Pd nanoarchitectures using an atomistic quantum-mechanical modelling approach. We have found that Au-Pd antenna-reactor systems exhibit significantly higher hot-carrier generation rates than core-shell nanoparticles. This is caused by the large electric field enhancements due to the localized plasmon mode associated with the gap between the antenna and the satellite nanoparticles. In particular, the largest overall hot-carrier generation rate is found for an antenna-reactor system in which the satellite is a core-shell nanoparticle. For the antenna-reactor systems, we also studied the dependence of the hot-carrier generation rates on the size of the gap, the radius of the antenna nanoparticle and the light polarization direction. We find that the largest rates are found when the electric field is parallel to the axis

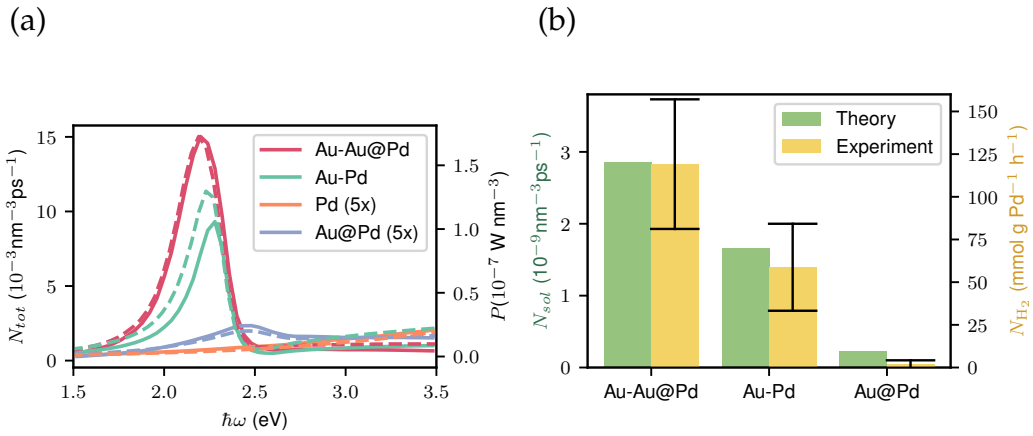

Figure 4.8: (a) Total hot carrier generation rate as a function of photon energy (averaged over all polarisation vectors) for a spherical Pd nanoparticle, an Au@Pd core-shell nanoparticle, an Au-Pd reactor and an Au-Au@Pd reactor. The power (per unit volume) absorbed by the Pd subsystem is shown in dashed lines. Note that the curves for the Pd nanoparticles and the Au@Pd have been multiplied by a factor of 5 to improve visibility. (b) Comparison of the measured difference in H_2 production upon illumination by a solar simulator [141] and in the dark to the calculated number of hot holes excited by solar illumination.

connecting the centres of the antenna and satellite nanoparticles. Also, small gaps and large antenna sizes favour hot-carrier generation. Comparing our calculated hot-carrier generation rates for the different Au-Pd photocatalysts to experimentally measured H_2 production rates, we find a strong correlation between theory and experiment. The insights from our work can guide the development of highly efficient heterogeneous hot-carrier nanodevices for energy conversion applications.

Chapter 5

Janus Nanoparticles

5.1 Introduction

Janus Nanoparticles are nanoparticles whose left half consists of a different material than their right half, as schematically shown in Figure 5.2 (a). These Janus nanomaterials have the ability to absorb light in different regions of the solar spectrum and, hence, enhance the performance of plasmonic devices. Depending on the synthesis method, some Janus nanoparticles synthesized in the laboratories are not spherical: they have a dumbbell shape, as shown in Figure 5.2(b)-(d). These nanoparticles have some unique properties and might enhance the photocatalytic performance.

Little is known experimentally about which combination of materials in Janus nanoparticles has optimal photocatalytic performance in terms of catalytic reactions, since synthesising all the combinations of Janus materials is time-consuming. Thus, it is important for computer simulations to help guide the experimental study.

The energy distribution of hot carriers is important for the photocatalytic performance of hot-carrier devices. For example, the presence of energetic 'hot' carriers could trigger chemical reactions that are unlikely to happen under ambient conditions. Our previous work (see chapter 4) suggests there is a strong correlation between the generation rate of hot carriers and the photocatalytic performance.

The hot-carrier distribution can be computed using the method discussed in the previous section. However, it is hard to find tight-binding parameters for complicated structures. For example, little research exists on tight-binding parameters of hetero-junctions. Hegde and coworkers[146] have attempted to model a gold-silver junction, but their work is only valid for bulk-like structures and with low strains. A

coherent gold-silver or silver-copper junction has at least 100 atoms. This makes it very difficult to parameterise using the Slater-Koster scheme. Other possible methods involve using maximally localised Wannier function[148, 149, 147]. However, the hopping values obtained from this method decay very slowly with distance[60] and the linear scaling method is only achieved if the tight-binding Hamiltonian is sparse.

In this work, we used a trick to simplify the tight-binding parameterization process by introducing an additional parameter for the onsite correction term to each material in the Hamiltonian. The density of states from the tight-binding Hamiltonian agrees very well with the result from the density functional theory calculation. Based on these parameters, we have computed the hot-carrier distribution for Janus nanoparticles made of Au, Ag and Cu. Based on the hot-carrier distribution, we will use the number of 'energetic' carriers as a figure of merit and compare the photocatalytic performance of these Janus nanoparticles.

5.2 Fitting the Tight-binding Hamiltonian

To build the interface at the centre of the Janus nanoparticle, we strained the copper, gold and silver slightly and then stacked them together to form a coherent interface[150] (with a strain of less than 1%). For each strained unit cell, we find its own set of tight-binding parameters using the method described in section 2.1.3. We average the hopping parameter of the two materials in the interface, and we only use the distance to determine whether the hopping is the first-nearest neighbour or second-nearest neighbour at the interface, but keep the hopping integral fixed. For each combination of materials, we add a constant to the onsite energy of each constituent material to include the fact that the pseudopotential can have an offset in the potential energy.

5.3 Results and Discussion

In this chapter, we study the spherical Janus nanoparticles and dumbbell-shaped Janus nanoparticles with necks. We define the neck size d as the separation of the upper and lower hemispheres' centre (of the equator). In this chapter, we study spherical Janus nanoparticles with a radius of 5 nm (containing 29,270 atoms for the gold-silver system, 36,393 for the gold-copper system and 36,498 atoms for the silver-copper system). We investigate neck sizes ranging from 2 nm to 6 nm (containing up to 65,458 atoms). The schematic illustration of the geometry for gold-silver Janus nanoparticles is shown in Figure 5.2(a)-(d). We define the z-axis

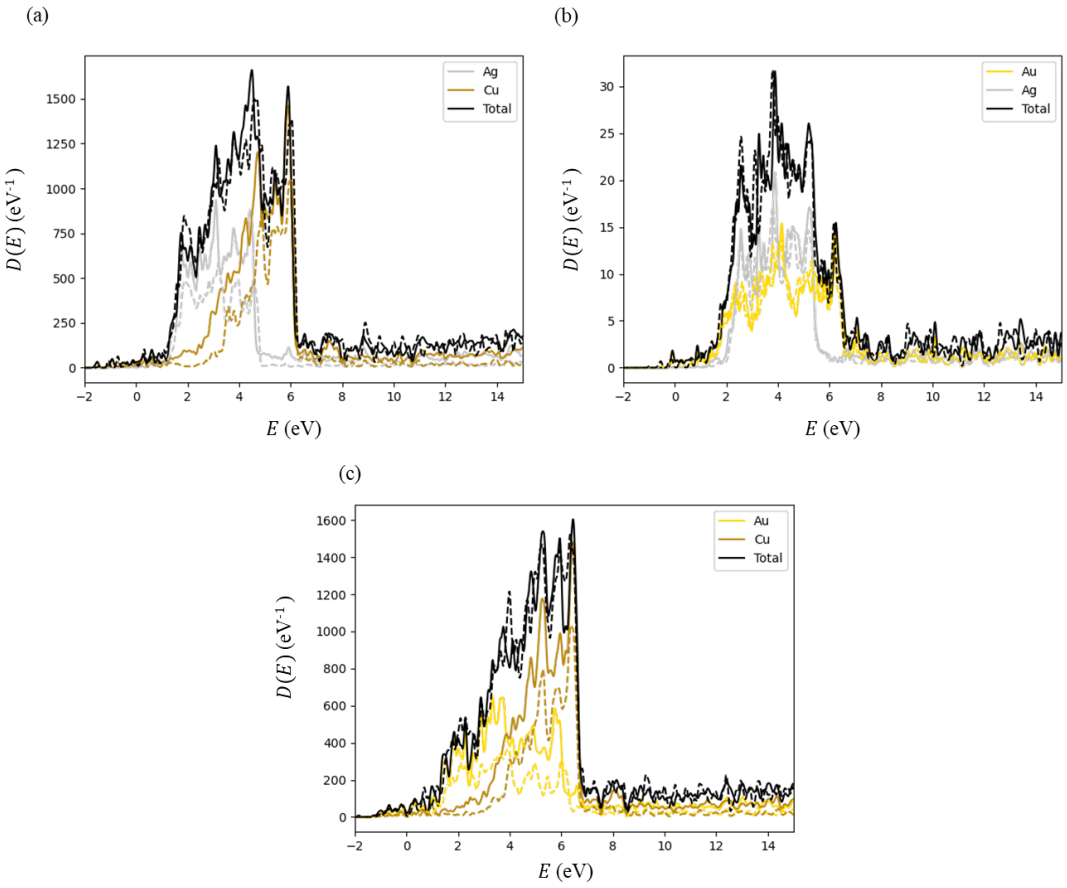

Figure 5.1: Schematic illustration of the density of states and density of states projected onto each material [151] for (a) Cu-Ag system, (b) Au-Ag system, and (c) Cu-Au system. The solid line corresponds to the tight-binding result, and the dashed line corresponds to the DFT result.

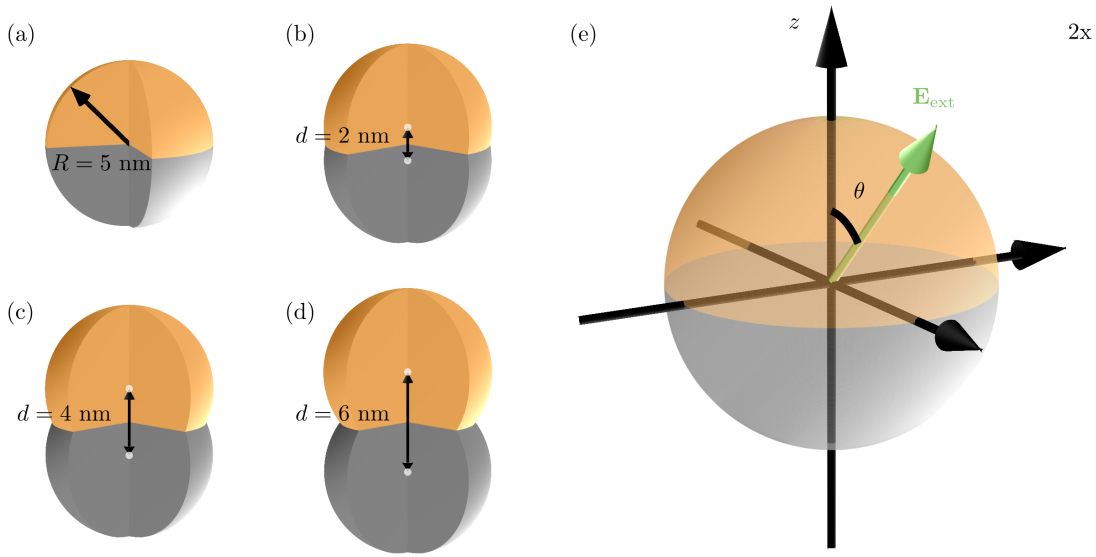

Figure 5.2: Schematic illustration of the geometry of Au-Ag nanoparticles studied in this article.

as the normal to the Janus nanoparticle interface and the polarisation angle θ as the angle made between the z-axis and the external field $\mathbf{E}_{\text{ext}}$; this is illustrated in figure 5.2(e).

5.3.1 Spherical Janus nanoparticles

In figure 5.3, we show the number of electrons and holes for the different Janus nanoparticles. We found that the electrons and holes generation rate reaches a maximum of around 3.4 eV, corresponding to silver's LSP frequency. Hence, with fixed illumination, silver and gold have the highest electron/hole generation rates among all the Janus nanoparticles. There are two important peaks in the systems: one is at 2.4 eV (green light), which corresponds to the resonance of gold. The other one is at 3.4 eV (ultraviolet light), corresponding to the resonance of silver nanoparticles, making the gold-silver have the largest enhancement in both cases. The polarization of the light greatly enhances the silver resonance peak, while it is less important for the gold resonance. For the silver peak at 3.4 eV, the generation rate is enhanced by a factor of 1.98(for electrons) and 1.15(for holes) when the light is perpendicular to the Janus interface ($\theta = 0°$) compared to the case when the light is parallel to the interface ($\theta = 90°$). By contrast, the enhancement is 1.10(electrons) and 1.53(holes) for the gold resonance at 2.4 eV. In our previous work, we found that for these systems with cylindrical symmetry, the hot carrier rates vary sinusoidally with the polarisation angles. This implies that for a randomly polarised light, the average generation rate is the average of

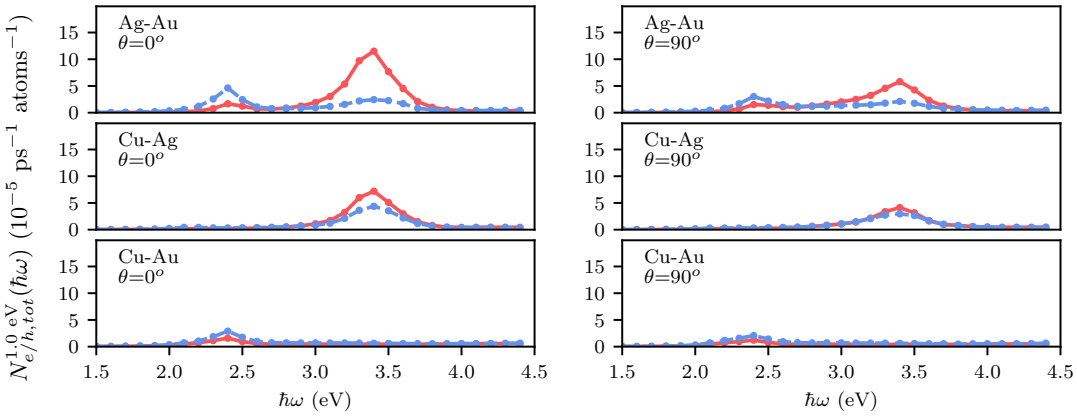

Figure 5.3: Variation of the number of electrons generated(red solid line) and holes generated(blue dashed line) with the energy of the incident light for Ag-Au, Cu-Ag and Cu-Au Janus nanoparticles.

the rate over the perpendicular polarisation and the two axes parallel to the Janus interface.

When we investigate the copper-silver combination, there is also a clear peak at 3.4 eV, but the magnitude of the peak is significantly smaller. However, there is no clear peak in the range of 2-3 eV. In section 3, we found that copper has a very weak peak in the range studied in this section. When the light is parallel to the Janus interface, the Cu-Ag performs similarly to the Au-Ag combination. However, the performance deteriorates when the light is parallel. At the frequency of 2.4 eV, the Cu-Au combination shows a clear peak. This peak is also weaker than the Au-Ag case for all polarisations.

The electron generation reaches a maximum at the LSP frequency of the constituent materials. In figure 5.4, we plot the hot-carrier generation rate when the LSP frequency of one of the constituent materials is reached. We found that the large hole peak was attributed to the d-band of Au, which is 2 eV below the Fermi level. The electrons were excited to the level just above Fermi's level, and the excited electron was very energetic. Similarly, copper also has some d-electrons at 2 eV below the Fermi level, but they are harder to excite at most of the visible light range, which results in a weaker photocatalytic performance.

5.3.2 Dumbbell-shaped Janus nanoparticles

So far, we found that Janus nanoparticles containing silver tend to generate the highest number of hot carriers for a fixed illumination in the near-ultraviolet regime. However, the intensity of the solar spectrum that corresponds to the gold/copper peak (red/green light) is higher. With this in mind, we investigate the effect of

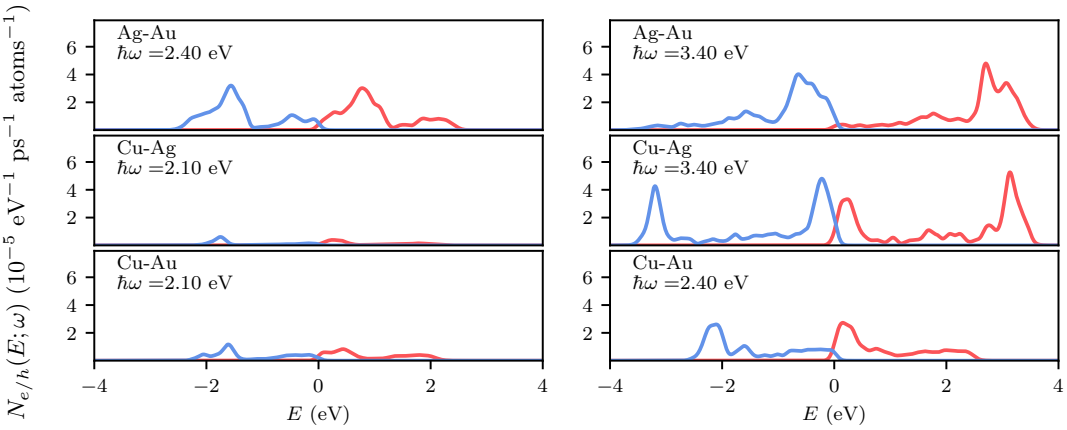

Figure 5.4: The hot carrier generation rate at the LSP frequency.

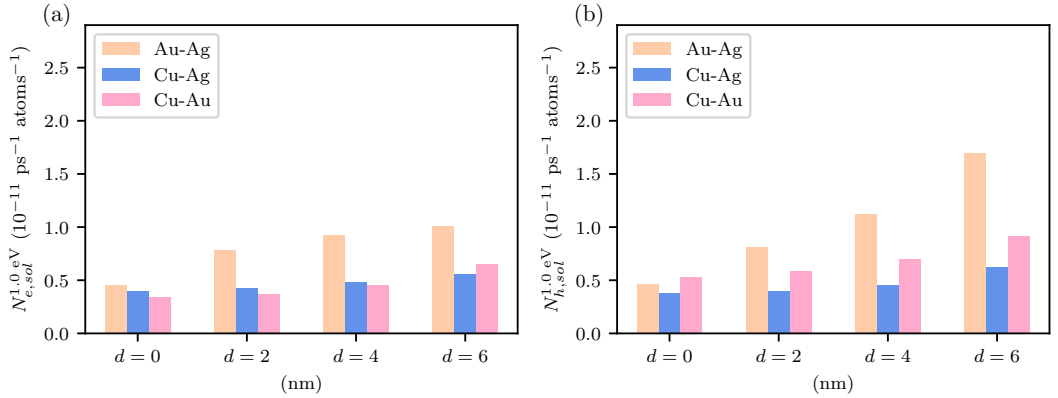

Figure 5.5: The dependency of neck size on the number of (a)electrons (b) holes generated when illuminated with the solar spectrum

neck size on the number of electrons/holes generated under solar illumination. It can be seen that the gold-silver Janus nanoparticle has the best overall performance among all combinations. When the neck size grows, the electron/hole generation rate grows, except for the case of electrons in the copper-silver system, where the rate remains constant. Amongst all the systems, the gold-silver system has the best overall performance with the largest improvement in the growth of neck size. From a spherical Janus nanoparticle to a Janus nanoparticle with d = 6 nm, the number of electrons generated grows by a factor of 2.22and the number of holes generated grows by a factor of 3.64.

To further understand the impact of neck size on photocatalytic performance, we studied the hot carrier distribution at the peak frequency for the gold-silver system. This is plotted in Figure 5.5. It can be seen that the silver peak at 3.6 eV does not have a significant enhancement. However, the gold peak gets significantly enhanced by a factor of 12.1(electrons) and 13.7(holes) from d = 0 nm to d = 6 nm. The resonance frequency also shifted from 2.4 eV to 2.1 eV. We plotted the hot carrier distribution in the right panel. It can be seen that the shape of the gold

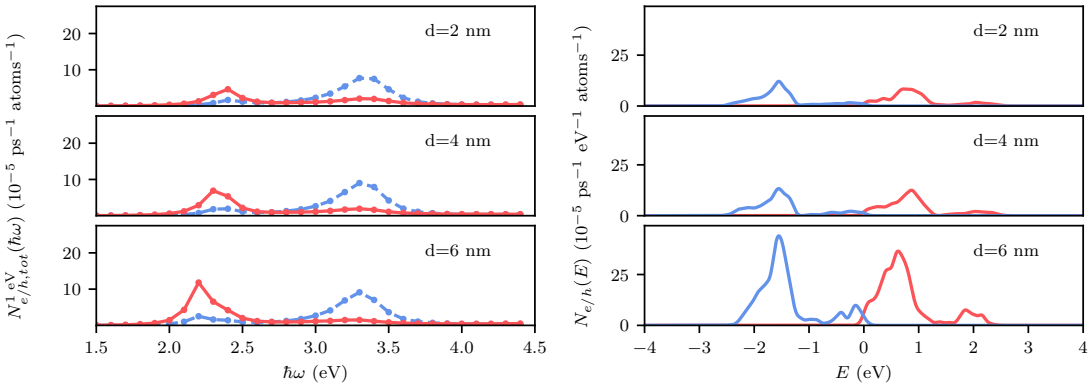

Figure 5.6: The dependence of gold-silver hot-carrier rate on the neck size.

peaks looks similar, but the magnitude of the sp-sp transition becomes larger. This is because a larger electric field $|\nabla\Phi_{tot}(\omega)|^2$ is induced at the neck region for the dumbell-shaped nanoparticle with sharper necks, as shown in figure 5.7.

Despite the fact that copper has weak plasmonic properties, it has good catalytic properties. Recently, research has shown that copper has superior performance in the CO_2 reduction reaction. [152] Hence, it is interesting to investigate the presence of gold and silver hemispheres on the hot carrier distribution of copper nanoparticles.

In figure 5.8, we plot the total number of hot electrons/holes generated under the effect of solar illumination. It can be seen that when the nanoparticles' neck size is large, gold enhances the hot electron and hot hole generation rate most significantly. However, for small neck sizes, the Cu-Au system generates fewer hot carriers, and the Cu-Ag system performs better. Overall, the Cu-Au system with a large neck size will have the best catalytic performance.

5.4 Conclusion

Overall, we have computationally investigated the hot-carrier generation and photocatalytic performance of gold-silver, gold-copper and silver-copper Janus nanoparticles. We found that the gold-silver Janus nanoparticles have the greatest performance. In particular, the gold part has a small electron peak at 2.4 eV, and silver has a large electron peak at 3.6 eV. We also found that the magnitude of the silver peak gets significantly enhanced when the polarisation of the light is perpendicular to the Janus interface. Then, we studied the performance of these Janus when the neck size changes, and we found that the gold peak has a significant contribution, as the intensity of the gold peak in the solar spectrum

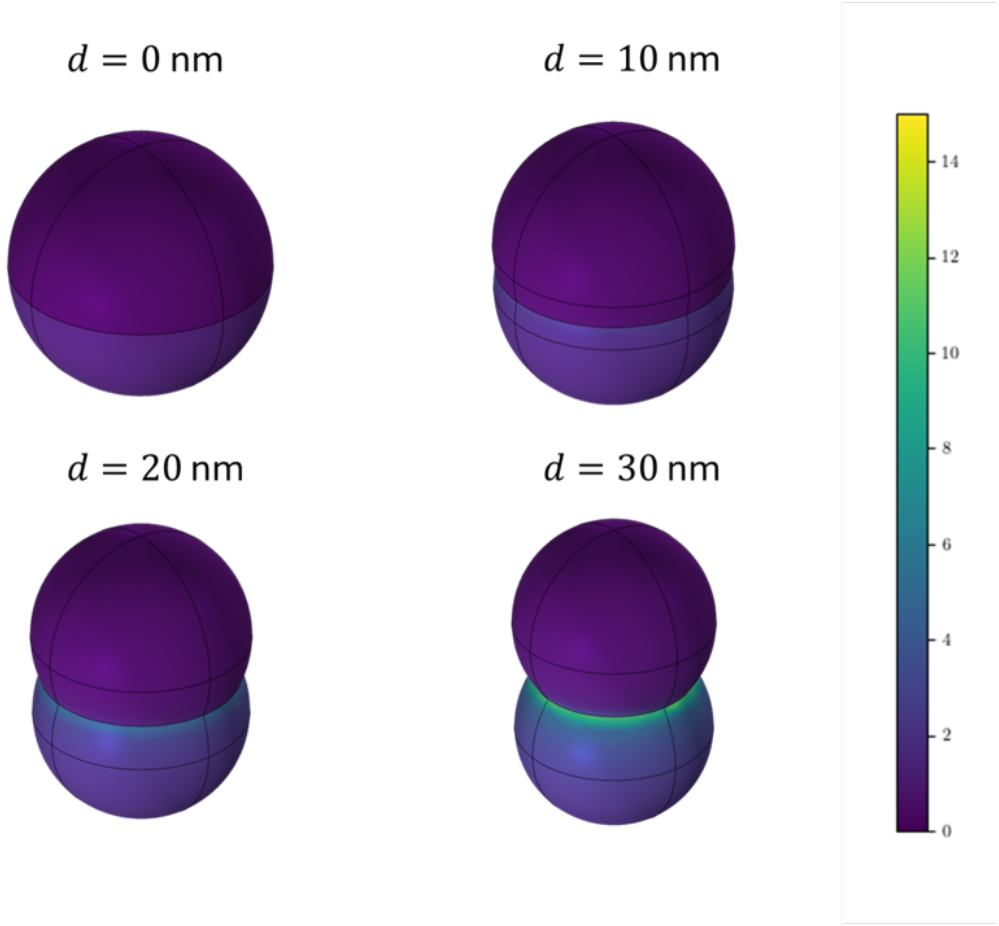

Figure 5.7: The electric field inside the Au-Ag Janus nanoparticle with different neck sizes (for $\hbar\omega = 2.4$ eV).

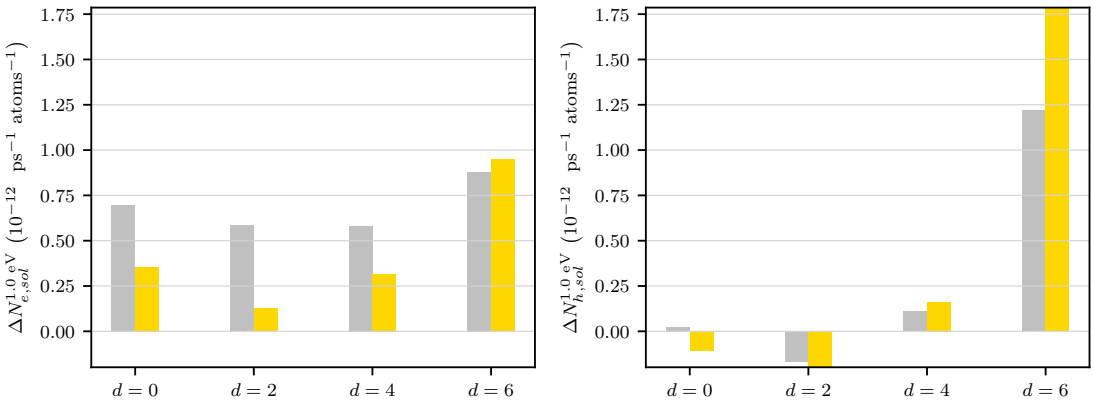

Figure 5.8: Schematic illustration of the excessive number of hot electrons or hot holes generated in copper with the effect of gold or silver neck size (compared with pure copper) under the illumination of the solar spectrum.

is high. We found that the gold peak gets significantly enhanced as the neck size increases. We have then investigated the hot carrier distribution for the dumbell-shaped nanoparticles at gold's resonance frequency. It was found that the peak contribution is due to field enhancement. These studies can speed up the discovery of new Janus photocatalytic materials.

Chapter 6

Conclusion

Overall, we developed a linear scaling kernel polynomial method to evaluate the hot-carrier generation rate in metallic nanoparticles. We used this method to model spherical gold, silver and copper nanoparticles and analysed the intraband and interband transition as the size of the nanoparticles increased. We found that there are more intraband transitions for smaller nanoparticles due to a larger surface-to-volume ratio. We also calculated the frequency dependence of the hot-carrier rate for very large nanoparticles (~ 30 nm). We found that near the resonance frequency, the magnitude of the hot-carrier generation peak gets enhanced significantly, but for higher frequencies, we can extract holes from d-bands that lie deeply below the Fermi level. Alternatively, we can extract energetic electrons that get excited to higher s-p bands.

We then used the linear-scaling method to study the palladium and palladium-gold core-shell nanoparticles (Pd and AuPd) and these nanoparticles surrounded by a spherical gold nanoparticle antenna (Au-AuPd, Au-Pd). We analysed the polarisation angle dependence of these systems and the frequency dependence of these systems. We found that the hot carrier generation rate of the palladium is significantly enhanced when the polarisation angle is parallel to the axis that joins the centre of two spheres. We also found that when the gap between the satellite and the antenna is small, the palladium generates a larger number of hot carriers. If the antenna size increases, the number of hot carriers generated in the palladium gets enhanced. We found a strong correlation between the total number of hot carriers generated and the photo-catalytical performance of these systems in the experiment.

Finally, we used our theory to predict the hot-carrier generation rate of Janus nanoparticles. We first compared the frequency and polarisation dependence

of the hot-carrier distribution for Au-Ag, Cu-Ag and Cu-Au nanoparticles. We found that the Au-Ag combination generates the highest number of hot carriers. We then studied dumbbell-shaped nanoparticles and investigated the effect of the separation of the centres of hemispheres on the hot-carrier generation rate. We found that the hot carrier generation of Au-Ag grows most rapidly when the centres separate. Copper is a good catalysis for certain reactions. We investigated the effect of Au and Ag on the enhancement of the copper part. We found that gold enhanced the copper hemisphere the most, provided that we separated the centres sufficiently.

6.1 Future Work

There are a few directions researchers can work in the future. For example, currently, the algorithm presented in this work can only be applied to calculate the hot-carrier generation rate (as discussed in section 2) and hot-carrier steady-state distribution (see reference [70]). This method could be generalised to calculate some other useful quantities. So far, we have only used the Slater-Koster tight-binding method, which limits the accuracy and types of the system that can be studied. Machine learning tight-binding methods are a rapidly growing research field [60]. Researchers can interface it with the method we have developed. Finally, we can develop a user-friendly code package that can be used by experimental scientists and allow them to find the connection between calculated hot-carrier properties and the experimental measurements.

6.2 Code availability

The code that can perform KPM calculation for hot-carrier distribution was available at https://github.com/Jlischner/MaxTB. It was originally developed by me, Simao Joao has made significant modifications to this code and created this repository, and it was then transferred to my supervisor, Johannes Lischner.

– Reference –

[1] G. Cao, *Nanostructures and Nanomaterials: Synthesis, Properties and Applications* (2004), Imperial College Press

[2] M. Faraday, Experimental relations of gold (and other metals) to lightPhil. Trans. R. Soc., **147**, 0 (1857)

[3] C. Clavero, Plasmon-Induced Hot-Electron Generation At Nanoparticle/Metal-Oxide Interfaces For Photovoltaic And Photocatalytic Devices, Nat. Photonics **8**, 95 (2014).

[4] U. Aslam, V. G. Rao, S. Chavez, and S. Linic, Catalytic Conversion Of Solar To Chemical Energy On Plasmonic Metal Nanostructures, Nat. Catalysis **1**, 656 (2018).

[5] S. Maier, *Plasmonics* (Springer US, Boston, 2007).

[6] A. M. Brown, R. Sundararaman, P. Narang, W. A. Goddard, and H. A. Atwater, Nonradiative Plasmon Decay And Hot Carrier Dynamics: Effects Of Phonons, Surfaces, And Geometry, ACS Nano **10**, 957 (2015).

[7] S. Link, and M. A. El-Sayed, Spectral Properties And Relaxation Dynamics Of Surface Plasmon Electronic Oscillations In Gold And Silver Nanodots And Nanorods, J. Phys. Chem. B **103**, 8410 (1999).

[8] M. L. Brongersma, N. J. Halas, and P. Nordlander, Plasmon-Induced Hot Carrier Science And Technology, Nat. Nanotechnol **10** (2015).

[9] A. Jiang, F. Wang, D. Xia, M. Li, L. Qiang, Z. Zhu, P. Wang, R. Fan, K. Lin , Y. Yang,Aluminum nanoparticles manufactured using a ball-milling method with ammonium chloride as a grinding aid: achieving energy release at low temperature, New J. Chem.,**43**, 1851-1856 (2019)

[10] C. L. Haynes, R. P. Van Duyne, Nanosphere Lithography: A Versatile Nanofabrication Tool for Studies of Size-Dependent Nanoparticle Optics, J. Phys. Chem. B , **105**, 24, (2001)

[11] J. Kimling, M. Maier, B. OkenveV. Kotaidis, H. Ballot, A. Plech, Turkevich Method for Gold Nanoparticle Synthesis Revisited, J. Phys. Chem. B , **110**, 32, (2006)

[12] R. S. Wagner, W. C. Ellis, Vapour-Liquid-Solid Mechanism of Single Crystal Growth, Appl. Phys. Lett. 4, 89–90 (1964)

[13] S. Szunerits, R. Boukherrouba, Sensing usinglocalisedd surface plasmon resonance sensors, Chem. Commun.,48, 8999-9010, (2012)

[14] V. Hodoroaba, W. Unger, A. Shard, *Characterization of Nanoparticles. Measurement Processes for Nanoparticles* (2019), Elsevier.

[15] S. K. Mulligan, J. A Speir, I. Razinkov, A. Cheng, J. Crum, T. Jain, E. Duggan, E. Liu, J. P Nolan, B. Carragher, C. S Potter, Multiplexed TEM Specimen Preparation and Analysis of Plasmonic Nanoparticles, Microscopy and Microanalysis, **21**, 4, (2015)

[16] Y. Zhao, H. Pan, Y. Lou, X. Qiu, J. Zhu, C. Burda, Plasmonic $Cu_{2-x}S$ Nanocrystals: Optical and Structural Properties of Copper-Deficient Copper(I) Sulfides, J. Am. Chem. Soc. , **131**, 12, (2009)

[17] X. Zhang, X. Wu, A. Centeno, M. P. Ryan, N. M. Alford, J. Riley , F. Xie, Significant Broadband Photocurrent Enhancement by Au-CZTS Core-Shell Nanostructured Photocathodes, Sci. Rep. **6**, 23364, (2016)

[18] G. Khitrova, P. R. Berman, M. Sargent, J. Opt. Soc. Am., **5**, 1, (1988)

[19] F. Enrichi, A. Quandt, and G. Righini, Plasmonic Enhanced Solar Cells: Summary Of Possible Strategies And Recent Results, Renew. Sust. Energ. Rev. **82**, 2433 (2018).

[20] A. O. Govorov, W. Zhang, T. Skeini, H. Richardson, J. Lee, and N. A. Kotov, Gold Nanoparticle Ensembles As Heaters And Actuators: Melting And Collective Plasmon Resonances, Nanoscale Res. Lett. **1**, 84 (2006) .

[21] G. V. Hartland, L. V. Besteiro, P. Johns, and A. O. Govorov, What'S So Hot About Electrons In Metal Nanoparticles?,ACS Energy Lett. **2**, 1641 (2017)

[22] E. Cortés, L. V. BesteiroAlessandro, A. B. TagliabueAngela, D Narang, Challenges in Plasmonic Catalysis,ACS Nano **14**, 12 (2020)

[23] A. FujiShima, and K. Honda, Electrochemical Photolysis Of Water At A Semiconductor Electrode, Nature **238**, 37 (1972).

[24] M. L. Salvador, B. A. MacLeod, A. Hess, A. P. Kulkarni, K. Munechika, J. I. L. Chen, and D. S. Ginger, Electron Accumulation On Metal Nanoparticles In Plasmon-Enhanced Organic Solar Cells, ACS Nano **6**, 10024 (2012).

[25] L. Yan, F. Wang, and S. Meng, Quantum Mode Selectivity Of Plasmon-Induced Water Splitting On Gold Nanoparticles, ACS Nano **10**, 5452 (2016).

[26] I. Thomann, B. Pinaud, Z. Chen, B. A. Clemens, T. F. Jaramillo, and M. L. Brongersma, Plasmon Enhanced Solar-To-Fuel Energy Conversion, Nano Lett. **11**, 3440 (2011).

[27] I. Goykhman, B. Desiatov, J. Khurgin, J. Shappir, and U. Levy, LocallyOxidisedd Silicon Surface-Plasmon Schottky Detector For Telecom Regime, Nano Lett. **11**, 2219 (2011).

[28] W. Li, and J. G. Valentine, Harvesting The Loss: Surface Plasmon-Based Hot Electron Photodetection, Nanophotonics **6**, 177 (2017).

[29] H. Chalabi, D. Schoen, and M. L. Brongersma, Hot-Electron Photodetection With A Plasmonic Nanostripe Antenna, Nano Lett. **14**, 1374 (2014).

[30] H. Tang, C. Chen, Z. Huang, J. Bright, G. Meng, R. Liu, and N. Wu, Plasmonic Hot Electrons For Sensing, Photodetection, And Solar Energy Applications: A Perspective, J. Chem. Phys. **152** , 220901 (2020).

[31] Q. Sun, C. Zhang, W. Shao, and X. Li, Photodetection By Hot Electrons Or Hot Holes: A Comparable Study On Physics And Performances, ACS Omega **4**, 6020 (2019).

[32] Y. Zhai, G. Chen, J. Ji, X. Ma, Z. Wu, Y. Li, and Q. Wang, Large-Scale, Broadband Absorber Based On Three-Dimensional Aluminum Nanospike Arrays Substrate For Surface Plasmon Induced Hot Electrons Photodetection, Nanotechnology **30**, 375201 (2019).

[33] Y. Zhu, H. Xu, P. Yu, and Z. Wang, Engineering Plasmonic Hot Carrier Dynamics Toward Efficient Photodetection, Appl. Phys. Rev. **8**, 021305 (2021).

[34] P. Reineck, G. P. Lee, D. Brick, M. Karg, P. Mulvaney, U. Bach, A Solid-State Plasmonic Solar Cell via Metal Nanoparticle Self-Assembly, Adv. Mat. **24**, 35 (2012)

[35] T. P. White , K. R. Catchpole, Plasmon-enhanced internal photoemission for photovoltaics: Theoretical efficiency limits, Appl. Phys. Lett., **101** (2012)

[36] Y. Dubi, I. W. Un, and Y. Sivan, Thermal effects – an alternative mechanism for plasmon-assisted photocatalysis, Chem. Sci. **11**, 5017 (2020).

[37] Y. Sivan, J. Baraban, I. Un, and Y. Dubi, Comment On "Quantifying Hot Carrier And Thermal Contributions In Plasmonic Photocatalysis", Science **364**, 6439 (2019).

[38] J. B. Khurgin, Hot Carriers Generated By Plasmons: Where Are They Generated And Where Do They Go From There?, Faraday Discuss. **214**, 35(2019).

[39] J. S. DuChene, G. Tagliabue, A. J. Welch, W. Cheng, and H. A. Atwater, Hot Hole Collection And Photoelectrochemical CO2 Reduction With Plasmonic Au/P-Gan Photocathodes, Nano Lett. **18**, 2545 (2018).

[40] G. Baffou, F. Cichos, and R. Quidant, Applications And Challenges Of Thermoplasmonics, Nat. Mater. , **19**, 946(2020).

[41] F. Giustino, *Materials Modelling using Density Functional Theory, Properties and Predictions* (2014), Oxford University Press

[42] P. Atkins, J. D. Paula, *Atkins' Physical Chemistry*, (2022), Oxford University Press.

[43] J. C. A. Prentice, J. A. James, C. Womack, A. E. A. Allen, L. Andrinopoulos, L. Anton, R. A. Bell, A. Bhandari, G. A. Bramley, R. J. Charlton, R. J. Clements, D. J. Cole, G. Constantinescu, F. Corsetti, S. M.-M. Dubois, K. K. B. Duff, J. M. Escartín, A. Greco, Q. Hill, L. P. Lee, E. Linscott, D. D. O'Regan, M. J. S. Phipps, L. E. Ratcliff, A. R. Serrano, E. W. Tait, G. Teobaldi, V. Vitale, N. Yeung, T. J. Zuehlsdorff, J. Dziedzic, P. D. Haynes, N. D. M. Hine, A. A. Mostofi, M. C. Payne, C. K. Skylaris, The `ONETEP` linear-scaling density functional theory program, J. Chem. Phys. **152**, 174111 (2020)

[44] J. Deslippe, G. Samsonidze, D. A. Strubbe, M. Jain, M. L. Cohen, S. G. Louie, BerkeleyGW: A massively parallel computer package for the calculation of the quasiparticle and optical properties of materials and nanostructures, Comp. Phys. Comm. **183**, 6 (2012)

[45] M. Bernardi, J. Mustafa, J. B. Neaton, and S. G. Louie, Theory And Computation Of Hot Carriers Generated By Surface Plasmon Polaritons In Noble Metals, Nat. Commun. **6**, 7044 (2015).

[46] L. R. Castellanos, O. Hess, and J. Lischner, Single Plasmon Hot Carrier Generation In Metallic Nanoparticles, Commun. Phys. **2**, 47 (2019).

[47] M. Kuisma, A. Sakko, T. P. Rossi, A. H. Larsen, J. Enkovaara, L. Lehtovaara, T. T. Rantala,Localisedd surface plasmon resonance in silver nanoparticles: Atomistic first-principles time-dependent density-functional theory calculationsPhys. Rev. B **91**, 115431 (2015)

[48] T. P. Rossi, and P. Erhart, M. Kuisma, Hot-Carrier Generation In Plasmonic Nanoparticles: The Importance Of Atomic Structure, ACS Nano **14**, 9963 (2020).

[49] R. Sundararaman, P. Narang, A. S. Jermyn, W. A. Goddard III, and H. A. Atwater, Theoretical Predictions For Hot-Carrier Generation From Surface Plasmon Decay, Nat. Commun. **5**, 5788 (2014).

[50] A. M. Brown, R. Sundararaman, P. Narang, W. A. Goddard, and H. A. Atwater, Ab Initiophonon Coupling And Optical Response Of Hot Electrons In Plasmonic Metals, Phys. Rev. B 94, 075120 (2016).

[51] J. Zhang, M. Guan, J. Lischner, S. Meng, and O. V. Prezhdo, Coexistence Of Different Charge-Transfer Mechanisms In The Hot-Carrier Dynamics Of Hybrid Plasmonic Nanomaterials, Nano Lett. **19**, 3187 (2019).

[52] A. Manjavacas, J. G. Liu, V. Kulkarni, and P. Nordlander, Plasmon-Induced Hot Carriers In Metallic Nanoparticles, ACS Nano **8**, 7630 (2014).

[53] S. D. Forno, Ranno, and L. Lischner, J. Material, Size, And Environment Dependence Of Plasmon-Induced Hot Carriers In Metallic Nanoparticles, J. Phys. Chem **122**, 8517(2018).

[54] M. Abramowitz, *Handbook of Mathematical Functions: With Formulas, Graphs, and Mathematical Tables* (2000), Dover Publications Inc

[55] L. Ranno, and S. D. Forno, J. Lischner, Computational Design Of Bimetallic Core-Shell Nanoparticles For Hot-Carrier Photocatalysis, Npj Comput. Mater. **4**, 31 (2018).

[56] L. R. Castellanos, J. Kahk, O. Hess, and J. Lischner, Generation Of Plasmonic Hot Carriers From D-Bands In Metallic Nanoparticles, J. Chem. Phys. **152**, 104111 (2020).

[57] W. A. Harrison, Tight-binding methods, Surf. Sci. **299**, 298, (1994)

[58] J. C. Slater, G. F. Koster, Simplified LCAO Method for the Periodic Potential Problem, Phys. Rev. **94**, 1498, (1954)

[59] D. Papaconstantopoulos, *Handbook of the band structure of elemental solids* (Springer, New York, 2015).

[60] C. Schattauer, M. Todorovic, K. Ghosh, P. Rinke and F. Libisch, Machine learning sparse tight-binding parameters for defectsnpj Comput Mater 8, 116 (2022).

[61] L. Shi, and D. Papaconstantopoulos, Modifications And Extensions To Harrison's Tight-Binding Theory, Phys. Rev. B **70**, 205101 (2004).

[62] S. M. João, M. Anđelković, L. Covaci, T. G. Rappoport, J. M. V. P. Lopes, and A. Ferreira, KITE: High-Performance Accurate Modelling Of Electronic Structure And Response Functions Of Large Molecules, Disordered Crystals And Heterostructures, R. Soc. Open Sci. **7**, 191809 (2020).

[63] S. M. João, and J. M. V. P. Lopes, Basis-Independent Spectral Methods For Non-Linear Optical Response In Arbitrary Tight-Binding Models, J. Condens. Matter Phys. **32**, 125901 (2019).

[64] A. Ferreira, and E. Mucciolo, Critical Delocalization Of Chiral Zero Energy Modes In Graphene, Phys. Rev. Lett. **115**, 106601 (2015).

[65] D. Jackson, *Über die Genauigkeit der Annäherung stetiger Funktionen durch ganze rationale Funktionen gegebenen Grades und trigonometrische Summen gegebener Ordnung*, (Dieterich, Göttingen, 1911)

[66] J. P. Boyd *Chebyshev & Fourier Spectral Methods* (Dover, 2001).

[67] A. Weiße, and G. Wellein, A. Alvermann, H Fehske, The Kernel Polynomial Method, RMP **78**, 275 (2006).

[68] **H. Jin**, M. Kahk, D. Papaconstantopoulos, A. Ferreira, J. Lischner, Plasmon-Induced Hot Carriers from Interband and Intraband Transitions in Large Noble Metal Nanoparticles, PRX Energy,**1**, 1 (2022).

[69] **H. Jin**, M. Herran, E. Cortés, J. Lischner, Theory of Hot-Carrier Generation in Bimetallic Plasmonic Catalysts, ACS Photonics, **10**, 10 (2023)

[70] S. M. Joao, **H. Jin**, J. Lischner, Atomistic Theory of Hot-Carrier Relaxation in Large Plasmonic Nanoparticles,J. Phys. Chem. C, **127**, 48 (2023)

[71] S. Ramachandran, S. M. João, **H Jin** , J. Lischner, Hot carriers from intra- and interband transitions in gold-silver alloy nanoparticles, Commun Chem, **7**, 169 (2024).

[72] P. A. M. Dirac, A new notation for quantum mechanics,Math. Proc. Camb. Philos. Soc., **35**, 3, (1939)

[73] David Tong: Quantum Mechanics, University of Cambridge, https://www.damtp.cam.ac.uk/user/tong/quantum.html, [Accessed 1/25/2025]

[74] David Tong: Principle of Quantum Mechanics, University of Cambridge, https://www.damtp.cam.ac.uk/user/dbs26/PQM.html, [Accessed 1/25/2025]

[75] D. Tong, *Quantum Mechanics*, (Cambridge University Press, 2025)

[76] H. J. Monkhorst and J. D. Pack, Special points for Brillouin-zone integrations, Phys. Rev. B, **13**, 5188 (1976).

[77] G. Kresse and J. Furthmuller, Efficient iterative schemes for *ab initio* total-energy calculations using a plane-wave basis set, Phys. Rev. B, **54**, 11169 (1996)

[78] G. Kresse and J. Furthmuller, Efficiency of ab-initio total energy calculations for metals and semiconductors using a plane-wave basis set, Comput. Mater. Sci., **6**, 1 (1994)

[79] J. P. Perdew, K. Burke, and M. Ernzerhof, Generalized Gradient Approximation Made Simple, Phys. Rev. Lett. **77**, 3865(1996).

[80] G. A. Watson, *Numerical Analysis, Proceedings of the Biennial Conference Held at Dundee* (Springer Berlin Heidelberg, Newyork, 1978).

[81] K. F. Garrity and K. Choudhary, Fast and accurate prediction of material properties with three-body tight-binding model for the periodic table, Phys. Rev. Materials **7**, 044603 (2023).

[82] J. J. Sakurai, J. Napolitano, *Modern Quantum Mechanics* (1985), Cambridge University Press.

[83] D. J. Griffth, D. F. Schroeter, *Introduction to Quantum Mechanics* (2018), Cambridge University Press

[84] O. Schnitzer, V. Giannini, R. V. Craster, S. A. Maier. Asymptotics of surface-plasmon redshift saturation at subnanometric separations, Phys. Rev. B **93**, 041409 (2016).

[85] O. Schnitzer. Singular perturbations approach to localised surface-plasmon resonance: Nearly touching metal nanospheres, Phys. Rev. B **92**, 235428 (2015)

[86] C. Bohern, *Absorption and Scattering of Light by Small Particles*(1998), WILEY

[87] M. Ruiz , O. Schnitzer. Plasmonic resonances of slender nanometallic rings, Phys. Rev. B **105**, 125412 (2022).

[88] O. Schnitzer. Asymptotic approximations for the plasmon resonances of nearly touching spheres, Eur. J. Appl. Math. **31**, 246 (2019)

[89] M. Ruiz, O. Schnitzer. Slender-body theory for plasmonic resonance, Proc. R. Soc **475**, 1471 (2019)

[90] D. J. Griffth, *Introduction to Electrodynamics* (2017), Cambridge University Press

[91] D. Tong *Electromagnetism* (2025), Cambridge University Press.

[92] D. Novko, V. Despoja, M. Reutzel, A. Li, H. Petek, and B. Gumhalter, Plasmonically assisted channels of photoemission from metals, Phys. Rev. B **103**, 205401 (2021)

[93] B. Gumhalter, D. Novko, and H. Petek, Electron emission from plasmonically induced Floquet bands at metal surfaces, Phys. Rev. B **106**, 035422 (2022)

[94] T. Pedersen, K. Pedersen, and T. B. Kriestensen, Optical Matrix Elements In Tight-Binding Calculations, Phys. Rev. B **63**, 201101 (2001).

[95] V. Blum, R. Gehrke, F. Hanke, P. Havu, V. Havu, X. Ren, K. Reuter, M. Scheffler, Ab Initio Molecular Simulations With Numeric Atom-Centered Orbitals, Comput. Phys. Commun. **180**, 2175 (2009).

[96] E. V. Lenthe, E. J. Baerends, and J. G. Snijders, Relativistic Total Energy Using Regular Approximations, J. Chem. Phys. , **101**, 9783(1994).

[97] Susanne Brenner, Ridgway Scott,*The Mathematical Theory of Finite Element Methods* (2007), Springer.

[98] Anders Bondeson, Thomas Rylander, Par Ingelstrom, *Computational Electromagnetics* (2006), Springer.

[99] Anders Logg, Kent-Andre Mardal, Garth Wells, *Automated Solution of Differential Equations by the Finite Element Method: The FEniCS Book: 84* (2012), Springer.

[100] Wolfgang Bangerth's video lecture, https://www.math.colostate.edu/~bangerth/videos.html[Accessed 1/25/2025]

[101] Imperial College London Finite elements, analysis and implementation lecture notes, https://finite-element.github.io/index.html [Accessed 1/25/2025]

[102] COMSOL Multiphysics® v. 6.1. www.comsol.com. COMSOL AB, Stockholm, Sweden.

[103] Antonio de Campos Pereira, Marcus Inacio , Hugo de Campos Pereira , Isabel Paiva, *COMSOL Multiphysics 5 - A Brief Introduction to CFD and Electromagnetism*(2020)

[104] Mehrzad Tabatabaian, *COMSOL for Engineers* (2014), Mercury Learning and Information

[105] H. William, *CRC handbook of chemistry and physics : a ready-reference book of chemical and physical data*, (CRC Press, Florida, 2015)

[106] Y. Saad and M. H. Schultz, GMRES: A Generalized Minimal Residual Algorithm for Solving Nonsymmetric Linear Systems, SISC, **7**, 3, (1986)

[107] Jennifer Scott, Miroslav Tuma , *Algorithms for Sparse Linear Systems* (2023), Springer.

[108] Imperial College London M3M6 Applied Complex Analysis lecture notes, available at https://github.com/dlfivefifty/M3M6AppliedComplexAnalysis [Accessed 1/27/2025]

[109] Vladimir I. Arnold, *Ordinary Differential Equations* (2006), Springer.

[110] Z. Bai, G. Fahey, G. Golub, Some large-scale matrix computation problems, J. Comput. Appl. Math., **74**, 1, (1996)

[111] Gilbert Strang, *Lecture Notes for Linear Algebra* (2021), Willey.

[112] K.F. Rilley, M.P. Hobson, S. J. Bence, *Mathematical Methods for Physics and Engineering* (2006), Cambridge University Press.

[113] Mark J. Ablowitz, Athanassios S. Fokas, *Complex Variables Introduction and Applications* (2003), Cambridge University Press.

[114] T. Mendes-Santos, M. Schmitt, and Ml Heyl, Phys. Rev. Lett. **131**, 046501 (2023)

[115] G. Rickayzen, *Green's Functions and Condensed Matter* (1984), Dover Books on Physics.

[116] L. Fox, I. B. Parker, *Chebyshev Polynomials in Numerical Analysis*, (1972), Oxford University Press.

[117] W. H. Press, S. A. Teukolsky, W. T. Vetterling, B. P. Flannery, *Numerical Recipes* (2007), Cambridge University Press.

[118] R.N. Silver, H. Roeder, A.F. Voter, J.D. Kress,Kernel Polynomial Approximations for Densities of States and Spectral Functions, J. Comput. Phys., **124**, 1 (1996)

[119] S. Goedecker, Linear scaling electronic structure methods, Rev. Mod. Phys. **71**, 1085 (1999)

[120] D. R. Bowler, T. Miyazaki, $\mathcal{O}(N)$ methods in electronic structure calculations, Rep. Prog. Phys. **75** 036503 (2012)

[121] T. Chen, A spectrum adaptive kernel polynomial method, J. Chem. Phys. **159**, 114101 (2023)

[122] M.F. Hutchinson, A stochastic estimator of the trace of the influence matrix for laplacian smoothing splines, Commun. Stat. - Simul. Comput., **19**, 2 (1990)

[123] K. Valerie , L. H. Viet, *2021, Symposium on Simplicity in Algorithms*(2021), Society for Industrial and Applied Mathematics.

[124] E. N. Epperly, J. A. Tropp , R. J. Webber, XTrace: Making the Most of Every Sample in Stochastic Trace Estimation, SIAM J. Matrix Anal. Appl., **45**, 1 (2024)

[125] Stochastic Trace Estimation - E. N. Epperly, https://www.ethanepperly.com/index.php/2023/01/26/stochastic-trace-estimation/ [Accessed 1/5/2025]

[126] J. Mikusiński, *The Bochner Integral* (1978), Birkhäuser Basel.

[127] II Probability and Measure lecture notes, https://dec41.user.srcf.net/h/II_M/probability_and_measure, [Accessed 1/25/2025]

[128] T. Iitaka, T. Ebisuzaki , Algorithm for Linear Response Functions at Finite Temperatures: Application to ESR Spectrum of $s = \frac{1}{2}$ Antiferromagnet Cu Benzoate, Phys. Rev. Lett. **90**, 047203

[129] David Skinner Mathematical Methods lecture notes, University of Cambridge, https://www.damtp.cam.ac.uk/user/dbs26/1Bmethods.html, [Accessed 1/25/2025]

[130] IB methods, https://dec41.user.srcf.net/h/IB_M/methods, [Accessed 1/25/2025]

[131] B. Y. Zheng, H. Zhao, A. Manjavacas, M. McClain, P. Nordlander and N. J. Halas, Distinguishing between plasmon-induced and photoexcited carriers in a device geometry, N. Commun. **6**, 7797 (2015)

[132] National Renewable Energy Laboratory(NREL) Homepage, https://www.nrel.gov/,[Accessed 1/25/2025]

[133] J. J. Mortensen, et. al., GPAW: An open Python package for electronic structure calculations, J. Chem. Phys. **160**, 092503 (2024)

[134] L. R. Castellanos, O. Hess, and J. Lischner, Dielectric Engineering Of Hot-Carrier Generation By Quantized Plasmons In Embedded Silver Nanoparticles, J. Phys. Chem, **125**, 3081 (2021).

[135] S. Ezendam, M. Herran, L. Nan, C. Gruber, Y. Kang, F. Gröbmeyer, R. Lin, J. Gargiulo, A. Sousa-Castillo, E. Cortés, Hybrid Plasmonic Nanomaterials for Hydrogen Generation and Carbon Dioxide Reduction, ACS Energy Lett. **7**, 2 (2022)

[136] A Chauhan, M. Rastogi , P. Scheier , C. Bowen , R. V. Kumar , R. Vaish, Janus nanostructures for heterogeneous photocatalysis, Appl. Phys. Rev. **5**, 041111 (2018).

[137] B. Hammer , J. K. Norskov , Why gold is the noblest of all the metals, Nature **376**, 238–240 (1995)

[138] V. G. Rao, U. Aslam, S Linic, Chemical Requirement for Extracting Energetic Charge Carriers from Plasmonic Metal Nanoparticles to Perform Electron-Transfer Reactions, J. Am. Chem. Soc. **141**, 1 (2019)

[139] S. Chavez, U. Aslam, S. Linic, Design Principles for Directing Energy and Energetic Charge Flow in Multicomponent Plasmonic, NanostructuresJ. Am. Chem. Soc. **141**, 1 (2019)

[140] N. Zohar, L. Chuntonov, G. Haran, The simplest plasmonic molecules: Metal nanoparticle dimers and trimers. J. Photochem. Photobiol. C, **21**, 26-39 (2014)

[141] M. Herran, A. Sousa-Castillo, C. Fan, S. Lee, W. Xie, M. Döblinger, B. Auguié, E. Cortés, Tailoring Plasmonic Bimetallic Nanocatalysts Toward Sunlight-Driven H2 Production Adv. Funct. Mater. **32**, 38 (2022).

[142] C. Zhan , Q. Wang , J. Yi , L. Chen , D. Wu , Y. Wang , Z. Xie , M. Moskovits , Z. Tian, Plasmonic nanoreactors regulating selective oxidation by energetic electrons and nanoconfined thermal fields,Sci. Adv. , **7**, 10 (2021).

[143] C. Engelbrekt, K. T. Crampton, D. A. Fishman, M. Law, V. Ara Apkarian, Efficient Plasmon-Mediated Energy Funneling to the Surface of Au@Pt Core–Shell Nanocrystals, ACS Nano, **14**, 4 (2020)

[144] U. Aslam, S. Chavez , S. Linic, Controlling energy flow in multimetallic nanostructures for plasmonic catalysis, Nature Nanotech 12, 1000–1005 (2017)

[145] J. J. Baumberg, J. Aizpurua, M. H. Mikkelsen , D. R. Smith, Extreme nanophotonics from ultrathin metallic gaps, Nat. Mater. **18**, 668–678 (2019)

[146] G. Hegde, M. Povolotskyi, T. Kubis, T. Boykin, G. Klimeck, An environment-dependent semi-empirical tight-binding model suitable for electron transport in bulk metals, metal alloys, metallic interfaces, and metallic nanostructures. I. Model and validation, J. Appl. Phys., **115**, 12 (2014).

[147] N. Marzari, A. Mostofi, J. Yates , I. Souza, D. Vanderbilt, Maximally localized Wannier functions: Theory and applications, Rev. Mod. Phys., **84**, 119.

[148] A. Mostofi, J. Yates, Y. Lee, I. Souza, D. Vanderbilt, N. Marzari, wannier90: A tool for obtaining maximally-localised Wannier functions, Comput. Phys. Commun., **178**, 9 (2008).

[149] G. Pizzi, et. al., Wannier90 as a community code: new features and applications, J. Phys.: Condens. Matter, **32** ,165902.

[150] A. H. Larsen, J. J. Mortensen, J. Blomqvist, M. M. N. Groves, B. Hammer, C. Hargus, E. D. Hermes, P. C. Jennings, P. B. Jensen, J. Kermode, J. R. Kitchin, E. L. Kolsbjerg, J. Kubal, K. Kaasbjerg, S. Lysgaard, J. B. Maronsson, T. Maxson, T. Olsen, L. Pastewka, A. Peterson, C. Rostgaard, J. Schiøtz, O. Schütt, M. Strange, K. S. Thygesen, T. Vegge, L. Vilhelmsen, M. Walter, Z. Zeng, K. W. Jacobsen, J. Phys.: Condens. Matter, **29**, 273002,(2017)

[151] V. Wang, N. Xu, J. Liu, G. Tang, W. Geng, VASPKIT: A user-friendly interface facilitating high-throughput computing and analysis using VASP code, Comput. Phys. Commun., **267**, 108033, (2021)

[152] B. Yang, K. Liu, H. Li, C. Liu, J. Fu, H. Li, J. E. Huang, P. Ou, T. Alkayyali, C. Cai, Y. Duan, H. Liu, P. An, N. Zhang, W. Li, X. Qiu, C. Jia, J. Hu, L. Chai, Z. Lin, Y. Gao, M. Miyauchi, E. Cortés, S. A. Maier, M. Liu, Accelerating CO_2 Electroreduction to Multicarbon Products via Synergistic Electric–Thermal Field on Copper Nanoneedles, J. Am. Chem. Soc., **144**, 7 (2022)